POLITECNICO DI MILANO
Corso di Laurea Magistrale in Ingegneria dell'Automazione
Dipartimento di Elettronica Informazione e Bioingegneria

CONTROL OF A SPAR–BUOY FLOATING WIND TURBINE

Relatore: Prof. Alberto Leva
Correlatore: Prof. Emilio García Moreno

Tesi di Laurea di:
Mattia Valtorta, matricola 804403

Anno Accademico 2015–2016

Abstract

Floating wind turbines take advantage of the offshore wind force to produce a renewable and clean electric energy. Such systems offer a solution to overcome offshore barriers due to the deep water. Nevertheless, adopting a floater platform introduces an additional motion that must be taken into account in the control system, which aims at achieving a better efficiency and system longevity. In this work, the development, implementation and simulation of a multi-objectives state feedback obtained with a Linear Quadratic Regulator and Disturbance Accommodating controllers are addressed. The results are applied in simulation to a spar-buoy floating platform.

The spar-buoy platform achieves hydrostatic stability using a deep drafted ballast with three catenary mooring lines. The deep draft increases the platform roll and pitch inertias, reducing their respective natural frequency. This affects the DOFs choice in the control design. Adding the platform surge and the first tower fore-aft, a correct representation of the platform pitch response to the collective blade pitch is achieved. Simulation are carried out using a high-fidelity model obtained with FAST within MATLAB Simulink and the fatigue analysis is obtained according to design load case (DLC) 1.1 of the IEC 61400-3 standard for normal operation conditions.

The simulation results, compared to a gain scheduled PI controller, show that a multi-objective state feedback controller obtained with collective blade pitch is able to improve the rotor speed regulation, thus the power quality. Furthermore, it is able to reduce tower-base side-to-side bending fatigue load by an average of 15%. Disturbance Accommodating Controller using the collective blade pitch further improves the rotor speed regulation. The state feedback controller obtained with the individual blade pitch is able to improve the rotor speed regulation reducing the RMS value of the rotor speed error by an average of 69%. Moreover it is able to reduce tower-base fore-aft bending fatigue load by an average of 8%. Disturbance Accommodation Controller, using the individual blade pitch, is able to improve the rotor speed regulation, thus diminishing the RMS value of the generator power error by an average of 70%, a better power quality is obtained.

The performances achieved by creating asymmetric loads, over symmetric load, help in a better regulation of the rotor speed keeping a limited motion of the platform rotation about its pitch axis. Furthermore, individual blade pitch prevents the controller from conflict issues arising when rotor speed and platform pitch are regulated simultaneously.

Sommario

Le turbine eoliche galleggianti, destinate alla produzione di energia elettrica pulita sfruttando la forza del vento in mare aperto, offrono una soluzione realizzabile per superare gli ostacoli causati delle acque profonde. Il fatto di utilizzare un sistema galleggiante, introduce un ulteriore movimento che assume un aspetto rilevante al fine del controllo destinato al miglioramento del rendimento e della longevità del sistema. In questo progetto è stato affrontato lo sviluppo, l'implementazione e la simulazione di due controllori multi-obiettivo a retrazione dello stato. Il primo è stato ricavato utilizzando un regolatore lineare quadratico (LQR) e il secondo utilizzando un Disturbance Accommodation Control (DAC) finalizzato alla reiezione dei disturbi. Entrambi i controllori sono stati applicati a una piattaforma galleggiante di tipo Spar-Buoy.

Questa tipologia di piattaforma raggiunge la stabilità idrostatica per mezzo di un profondo pescaggio e tre linee di ancoraggio. La profondità del pescaggio aumenta le inerzie di rollio e beccheggio, riducendo le frequenze naturali della piattaforma, interagendo con la scelta dei gradi di libertà da considerare nel modello di controllo. Al fine di ottenere una corretta rappresentazione della risposta in frequenza del beccheggio della piattaforma è necessario considerarne l'avanzamento della stessa in direzione-x (surge) e il primo modo di vibrare della torre in direzione prua-poppa. Le simulazioni sono effettuate utilizzando un modello ad alta fedeltà ottenuto con il simulatore FAST e MATLAB Simulink. Rispettando le norme IEC 61400-3, l'analisi a fatica è ricavata utilizzando il disegno di carico (DLC 1.1) adottato per le normali condizioni operative.

I risultati delle simulazioni, comparati con un controllore PI a guadagno variabile, mostrano che un controllo multi-obbiettivo a retrazione dello stato, ottenuto con un beccheggio collettivo delle pale, migliora la regolazione della velocità del rotore e di conseguenza la qualità della potenza prodotta. Applicando questo controllo si riscontra, risultante dall'analisi a fatica, la riduzione media del 15% sul carico alla base della torre, in direzione lato-lato. Il controllore DAC, anch'esso realizzato con un controllo collettivo delle pale, evidenzia un ulteriore miglioramento nella regolazione della velocità di rotazione del rotore. Il controllore a retrazione dello stato, ottenuto con una regolazione individuale della pale, migliora la prestazione della velocità del rotore riducendo il valore RMS del 69%. In questo caso i carichi a fatica alla base della torre, in direzione prua-poppa, risultano ridotti del 8%. Il regolatore DAC, ottenuto con una regolazione individuale delle pale, migliora ulteriormente la performance del controllo di velocità, diminuendone il valore RMS del 70%.

Rispetto a carichi aerodinamici simmetrici, l'utilizzo di carichi asimmetrici permette una migliore regolazione della velocità del rotore mantenendo limitato il movimento di beccheggio della piattaforma. Inoltre, preserva il controllore da eventuali conflitti che sorgono durante la regolazione simultanea della velocità del rotore e il beccheggio della piattaforma.

To Emma

Contents

List of Figures

List of Tables

Chapter 1

Introduction

After the black gold of the 20th century, shall we discover blue gold in the 21st one? Only in theory oceans offer a wide range of renewable energy sources such as wind, tidal, wave and thermal, and those energies could hypothetically be used without any limits. Theoretically yes, but not necessarily in practice, given that each of those energies requires complex and expensive installations that are actually in conflict with other marine activities, such as fishing and tourism. This is the reason why we are facing a step-by-step growth of marine energy utilization.

1.1 Offshore Wind Energy

Today, the most mature, integrated and accomplished technology is offshore wind turbine. The principle is based on the installation of the wind turbines in the sea, where the wind is more abundant and consistent than on land. As stated in [2] by the European Wind Energy Association (EWEA), Europe's cumulative installed capacity at the end of 2015 reached 11027,3 MW, across a total of 3230 wind turbines. With installed capacity now producing approximately 40,6 TWh in a standard wind year, there is enough electricity from offshore wind to cover 1,5% of the EU's total electricity consumption. United Kingdom has the largest amount of installed offshore wind capacity (5060,5 MW) representing 45.9% of whole European installations. Germany and Denmark follow with 3294,6 MW (29.9%) and 1271,3 MW (11.5%), respectively. The remaining 12.7% belong to: Belgium, Netherlands, Sweden, Finland, Ireland, Spain, Norway and Portugal.

Most of these offshore wind turbines are located close to the coast, mounted on foundation in relatively shallow waters (less than 30 meters). Today, this method is well established. However, specialists are considering alternative equipment that would be installed further off the coast and enjoy even stronger and steadier wind: wind turbines on floating platforms. Gains from this type of installation are estimated at 500 hours of full-capacity operation per years. Even if this one is supposed to be sure a promising solution, it requires sophisticated technology to maintain the stability of the turbine/platform in rough seas or high wind. At the end of 2012 two full scale grid connected offshore wind turbines on floating substructure are installed: Hywind and Windfloat.

They are both located in Europe, one in the North Sea and one in the Atlantic Ocean. Today seven experimental floating substructures (four in Europe, two in Japan and one in the United States) are in a test phase. In year 2014, after five years testing on the Hywind prototype, Statoil deployed the Hywind Scotland Pilot Park [31], which will be completed in the year 2017. The park will include five Hywind wind-turbine generator units with a total maximum capacity of up to 30 MW.

Numerous floating platform concepts are available for offshore wind turbines. Figure (1.1) represents the three mains: ballast stabilized (Spar–Buoy), mooring line stabilized (Tension Leg Platform) and buoyancy stabilized (Barge).
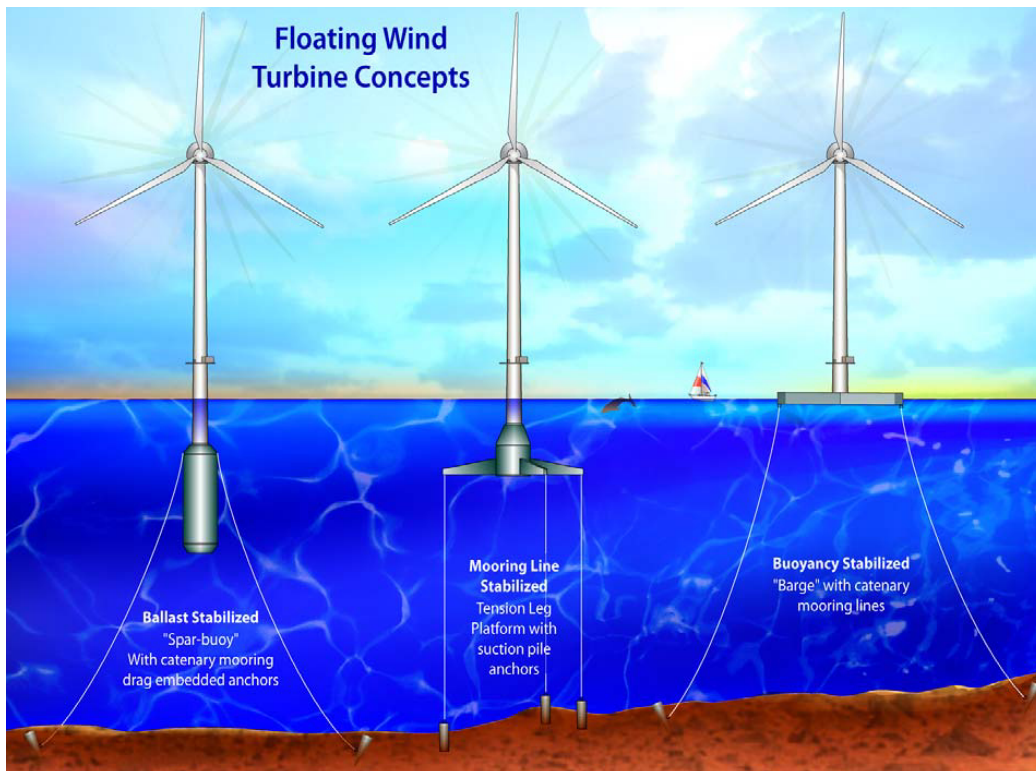
Figure 1.1: Mains Floating Platform Concepts for Offshore Wind Turbines

In this dissertation a spar-buoy platform model has been considered: more precisely the OC3-Hywind model developed from Phase IV of the OC3 project and based on the Hywind model defined in [22]. This concept has been chosen due to its simple design, to its suitability to modelling and to its propinquity to commercialization.

1.2　Thesis Objectives

In collaboration with the Universidad Politécnica de Valencia (UPV), with the aim of analysing different control strategies, a study has been adopted using two different control mechanisms:

- Collective Blade Pitch

- Individual Blade Pitch

The main purpose is to quantify the performance of different control systems aiming at achieving a better rotor speed regulation, thus a better power quality. Another important objective is the reduction in tower loads, given by the decrease of the platform motions.

In this thesis two multi-objective controllers are applied to spar-buoy platform concept to improve the system performances: i) State Feedback Control (SFC), obtained with a Linear Quadratic Regulator (LQR), and ii) Disturbance Accommodation Control (DAC). These controllers are compared with a baseline Gain Scheduled PI (GSPI) used as reference. Furthermore ten performance indices are used to evaluate the control quality (see Chapter 6 for more details).

Design Load Case (DLC) 1.1 in the IEC 61400-3 standard for offshore wind turbine is used to analyse the fatigue load performance under normal operating conditions (more details are given in Appendix B).

Simulations and control models are carried out using FAST (Fatigue, Aerodynamics, Structure and Turbulence) [19], a National Renewable Energy Laboratory (NREL) CAE tool to simulate the coupled dynamics response of wind turbines. It is used in conjunction with MATLAB Simulink for control design and implementation.

1.3　Thesis Outline

- Chapter 2 describes the wind and sea-wave models.

- Chapter 3 introduces the hydrodynamic model.

- Chapter 4 describes the aerodynamic model, the tower flexibility and the model actuators.

- Chapter 5 presents the control strategies and their implementation.

- Chapter 6 shows the comparative analysis between implemented controllers.

- Chapter 7 reports the work conclusions and further developments.

- Appendix A describes the linearized model obtained with FAST.

- Appendix B describes the the fatigue analysis.

Chapter 2

Wind and Wave Models

In this chapter the mathematical models used to develop the wind and the sea-waves are presented. In particular, the first part introduces the wind model, its turbulence intensity and its power-law profile. The wind speed represents the main exogenous signal with the biggest influence on a wind turbine. Therefore a detailed model ensures better control performances. The second part presents two sea-wave models. The first is used to describe fully developed seas, whereas the second is a fetch-limited version of the first.

2.1 Wind Model

The wind model has been developed with *TurbSim* [6], a stochastic, full-field, turbulent-wind simulator. TurbSim adopts a statistical approach instead of a physics-based model. It numerically simulates time series of three-component wind-speed vectors in a two-dimensional vertical rectangular grid that is fixed in space. TurbSim output will be used as input for *AeroDyn* [8].

2.2 Spectral Model

This section describes the velocity spectrum used in the model and discusses the measurements adopted to develop scaling for the site-specific model. Standard deviations, σ, have been calculated by integrating the velocity spectra, S:

$$\sigma^2 = \int_0^\infty S(f)\, dt, \tag{2.1}$$

2.2.1 Kaimal Model

The *IEC Kaimal* model has been defined in *2nd* and *3nd* edition of the *IEC 61400–1*. It assumes a neutral atmospheric stability while the velocity spectra for u, v and w wind components are given by:

$$S_k(f) = \frac{4\sigma_K^2 L_K / \bar{u}_{hub}}{(1 + 6 f L_K / \bar{u}_{hub})^{\frac{5}{3}}} \qquad for\ K = u,\ v,\ w \tag{2.2}$$

where $\bar{u}_{hub}$ is the mean wind speed, f is the cyclic frequency and L_K is the integral scale parameter defined as follows:

$$L_K = \begin{cases} 8.10\Lambda_U, & K = u, \\ 2.70\Lambda_U, & K = v, \\ 0.66\Lambda_U, & K = w \end{cases} \qquad (2.3)$$

where the turbulence parameter (Λ_U) can be described as indicated in equation (2.4).

$$\Lambda_U = \begin{cases} 0.7\,min(30m, HubHt), & Edition\,2 \\ 0.7\,min(60m, HubHt), & Edition\,3 \end{cases} \qquad (2.4)$$

The relationships between the standard deviations are defined as:

$$\begin{aligned} \sigma_v &= 0.8\sigma_u \\ \sigma_w &= 0.5\sigma_u \end{aligned} \qquad (2.5)$$

Both the velocity spectra and the standard deviations are assumed to be invariant across the grid. The effect is a small variation of the u-component standard deviation due to the spatial coherence model (not specified here).

(a) (b)
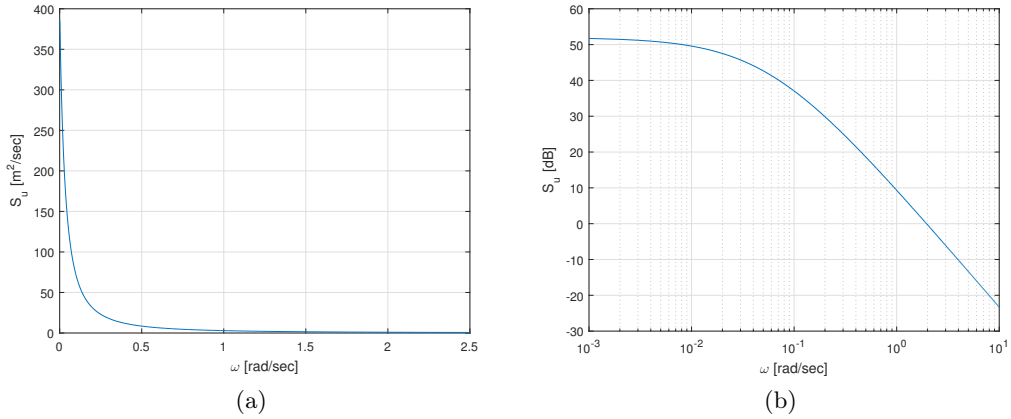
Figure 2.1: Kaimal Spectrum for u-component

2.3 Turbulence Intensity

The description of the turbulent component has been provided adopting a Normal Turbulence Model (NTM) in conjunction with the *IEC Kaimal* model.
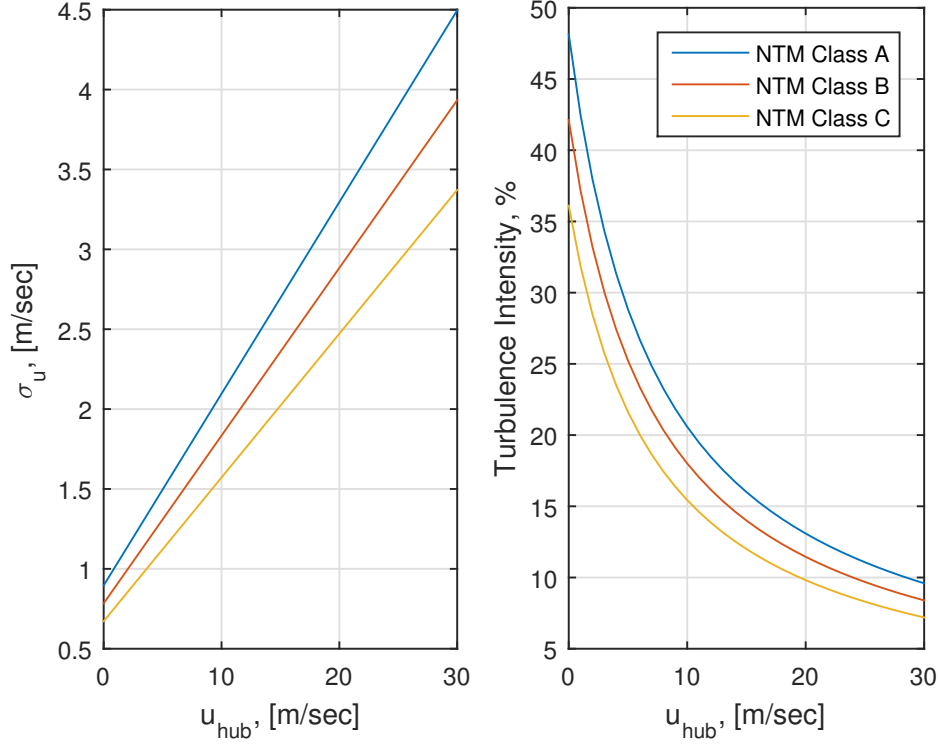
Figure 2.2: Longitudinal wind-speed standard deviation and turbulence intensity (TI) categories

The standard deviation of the u-component, σ_u can be approximated using the following relationship:

$$\hat{\sigma}_u = \sigma_u = I_{ref}(0.75\,\bar{u}_{hub} + 5.6) \tag{2.6}$$

where, I_{ref} is the expected value of turbulence intensity at $15\,m/s$.

The standards are:

- 16% for *Class A*

- 14% for *Class B*

- 12% for *Class C*

In this model, $I_{ref} = 0.14$, namely the B category, has been used for equation (2.6).

Table (2.1) summarizes the parameters used to create the wind spectral model.

	Parameters List	
$\bar{u}_{\text{hub}}$	18.0	m/sec
Λ_U	42.0	m
L_u	340.20	m
L_v	113.40	m
L_w	27.72	m
σ_u	2.674	m/sec
σ_v	2.139	m/sec
σ_w	1.337	m/sec
Z_0	0.03	m
$PLExp$	0.14	-

Table 2.1: Wind Model Parameters

2.4 Wind Profiles

The velocity profiles determine the mean u-component velocity at each height. By default, the mean w- and v-component velocities are zero. To comply with the *IEC* standard (IEC 61400–3) the power-law and logarithmic wind profiles have been adopted. The first has been used for rotor disk, the second elsewhere.

2.4.1 Power-Law Wind Profile

The equation (2.7) defines the wind profile on rotor disk. It uses a *PLExp* input parameter to calculate the average wind speed at height z.

$$\bar{u}(z) = \bar{u}(z_{ref})\left(\frac{z}{z_{ref}}\right)^{PLExp} \tag{2.7}$$

where $\bar{u}(z)$ is the mean wind speed at height z and z_{ref} is the reference height above still water, where the mean wind speed $\bar{u}(z_{ref})$ is known.

2.4.2 Logarithmic Wind Profile

The logarithmic wind profile calculates the average wind speed at height z, using the following trend:

$$\bar{u}(z) = \bar{u}(z_{ref})\frac{\ln(\frac{z}{Z_0}) - \gamma_m}{\ln(\frac{z_{ref}}{Z_0}) - \gamma_m} \tag{2.8}$$

where z is the height above the ground, z_{ref} is the height where the mean wind speed is known, Z_0 is the input surface roughness, $\bar{u}(z)$ is the mean wind speed at z and γ_m is a function that varies according to the *Gradient Richardson Number* (*GRN*). In particular γ_m is equal to zero when $GRN = 0$. Using the IEC spectral model $GRN = 0$, hence $\gamma_m = 0$.
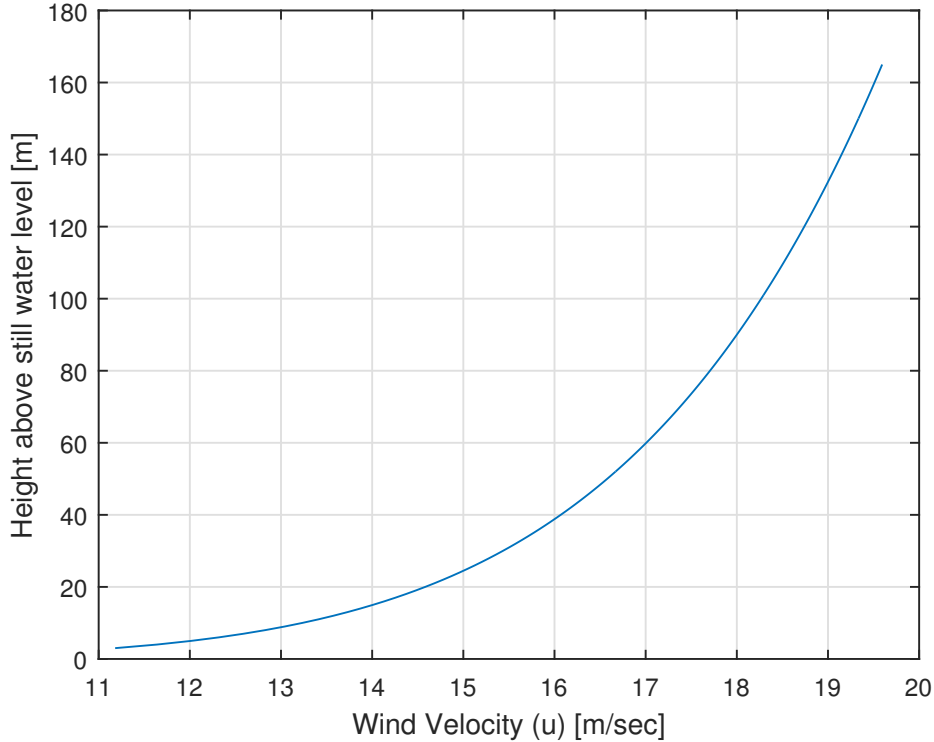
Figure 2.3: The Wind Speed profile generated from the combination of Power-Law and Logarithmic

2.4.3 Surface Roughness Length

The surface roughness length Z_0 measures the roughness of terrain surface or, as in this case, of the water surface. It can be also defined as the extrapolated height at which the mean wind speed becomes zero in a neutral atmosphere. As defined in the standard *IEC*, Z_0 has been assumed equal to 0.03.

2.5 Wave Model

In this section a mathematical model is built to represent the sea wave trend as in [23]. Then it is implemented within *HydroDyn*[20]. Marine waves have different length and period. Using a spectral representation, a simple sea wave model can be obtained. To describe the waves, the most famous spectra available in literature are:

- *Joint North Sea Wave Project (JONSWAP)*

- *Pierson–Moskowitz*

Both are presented in the IEC 61400–3 standard design as stated in [1].

The parameters characterizing a wave are: i) the peak spectral period of incident waves, T_p calculated as $(1/f_p)$, where f_p is the peak frequency in the spectral distribution and, ii) the significant wave height of incident waves, H_s,

defined as 1/3 of the largest waves height observed over a period. Another important parameter is the *fetch*. It describes the ocean area over the wind blows with a constant intensity and direction, thus generating waves. The *Pierson-Moskowitz* wave spectrum is generally used to describe the statistical properties of fully developed seas. On the contrary, the JONSWAP spectrum is normally used in a limited fetch situation.

2.5.1 JONSWAP Spectrum

The JONSWAP (Joint North Sea Wave Project) spectrum, defined in [32], is an empirical relationship that defines the distribution of energy with frequency within the ocean. It is a fetch-limited version of the *Pierson-Moskowitz* spectrum. The wave spectrum is never fully developed and may continue developing due to non-linear wave-wave interactions that emerge for a very long period of time. As a consequence, in the JONSWAP spectrum, waves continue to grow with distance.

The one-sided power spectral density is defined as:

$$S_\zeta^{\text{1-Sided}}(\omega) = \frac{1}{2\pi}\frac{5}{16}H_s^2 T_p \left(\frac{\omega T_p}{2\pi}\right)^{-5}\exp\left[-\frac{5}{4}\left(\frac{\omega T_p}{2\pi}\right)^{-4}\right][1-0.287\ln\gamma]\gamma^{\exp\left\{-0.5\left[\frac{\frac{\omega T_p}{2\pi}-1}{\sigma(\omega)}\right]^2\right\}}$$

(2.9)

where, T_s and H_s are defined above, σ is a scaling factor and γ is the peak shape parameter of a given irregular sea state. As suggested by the IEC 61400-3 standard design, the peak shape parameter and the scaling factor can be derived from H_s and T_p, as follows:

$$\gamma = \begin{cases} 5 & for\ \frac{T_p}{\sqrt{H_s}} \leq 3.6 \\ \exp\left(5.75 - 1.15\frac{T_p}{\sqrt{H_s}}\right) & for\ 3.6 < \frac{T_p}{\sqrt{H_s}} \leq 5 \\ 1 & for\ \frac{T_p}{\sqrt{H_s}} > 5 \end{cases}$$

(2.10)

and

$$\sigma(\omega) = \begin{cases} 0.07 & for\ \omega \leq \frac{2\pi}{T_p} \\ 0.09 & for\ \omega > \frac{2\pi}{T_p} \end{cases}$$

(2.11)

In (2.10), H_s and T_p must have units of meters and seconds, respectively.

When $\gamma = 1$ in (2.10), the one-sided JONSWAP spectrum formulation of (2.9) reduces to the one-sided *Pierson-Moskowitz* spectrum, as given in (2.12).

2.5.2 Pierson-Moskowitz Spectrum

The *Pierson-Moskowitz* spectrum, as mentioned above, is used to describe statistical properties of fully developed seas.

The spectrum obtained in frequency is:

$$S_\zeta^{\text{1-Sided}}(\omega) = \frac{1}{2\pi}\frac{5}{16}H_s^2 T_p \left(\frac{\omega T_p}{2\pi}\right)^{-5}\exp\left[-\frac{5}{4}\left(\frac{\omega T_p}{2\pi}\right)^{-4}\right]$$

(2.12)

where T_s and H_s are the same parameters reported in equation (2.9).

In the *Pierson-Moskowitz* spectrum, waves are generated from the wind speed. Therefore, it emerges as necessary to express the parameters H_s and T_p as functions of v, as introduced in eqs. (2.13) and (2.14):

$$H_s = \frac{2}{g}\sqrt{\frac{\alpha}{\beta}}v_{19.5}^2 \tag{2.13}$$

and

$$f_p^4 = \frac{4}{5}\beta\left(\frac{g}{2\pi v_{19.5}}\right)^4 \tag{2.14}$$

where g is the gravitational acceleration, $v_{19.5}$ is the wind speed at 19.5 meters of height above Still Water Level (SWL), while α and β are two dimensionless experimental constants equal to 0.0081 and 0.74, respectively.

From eqs. (2.13) and (2.14) it is deduced that:

$$T_p = \frac{1}{f_p} = \frac{2\pi v_{19.5}}{g}\left(\frac{5}{4\beta}\right)^{\frac{1}{4}} = \pi\left(\frac{5}{g^2\alpha}\right)^{\frac{1}{4}}H_s^{\frac{1}{2}} \tag{2.15}$$

The wave spectrum has been truncated above a cut-off frequency value. This is usually proportional to the peak spectral frequency. The adopted proportionally factor is 3.0 according to [23].

The parameters, shown in table (2.2), have been used to develop the wave model correlated to the wind model.

Parameter	Value	Units
$v_{19.5}$	15.56	m/sec
H_s	4.5	m
T_p	10.6	sec

Table 2.2: Wave Model Parameters
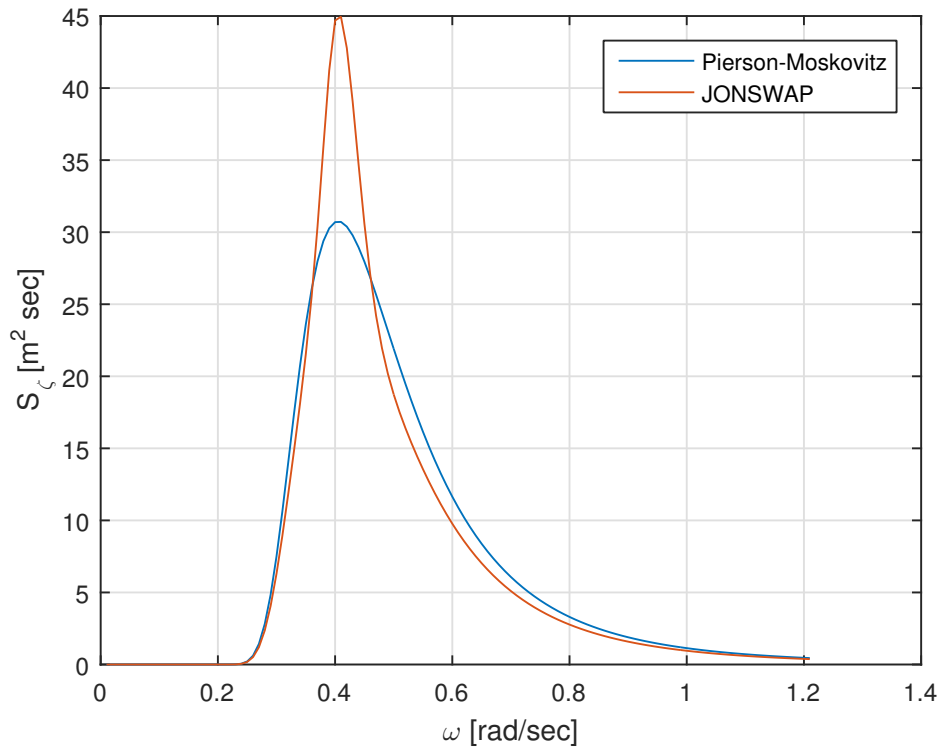
Figure 2.4: Comparison between *Pierson-Moskowitz* and JONSWAP spectra realized with $H_s = 11.8$ and $T_p = 15.5$
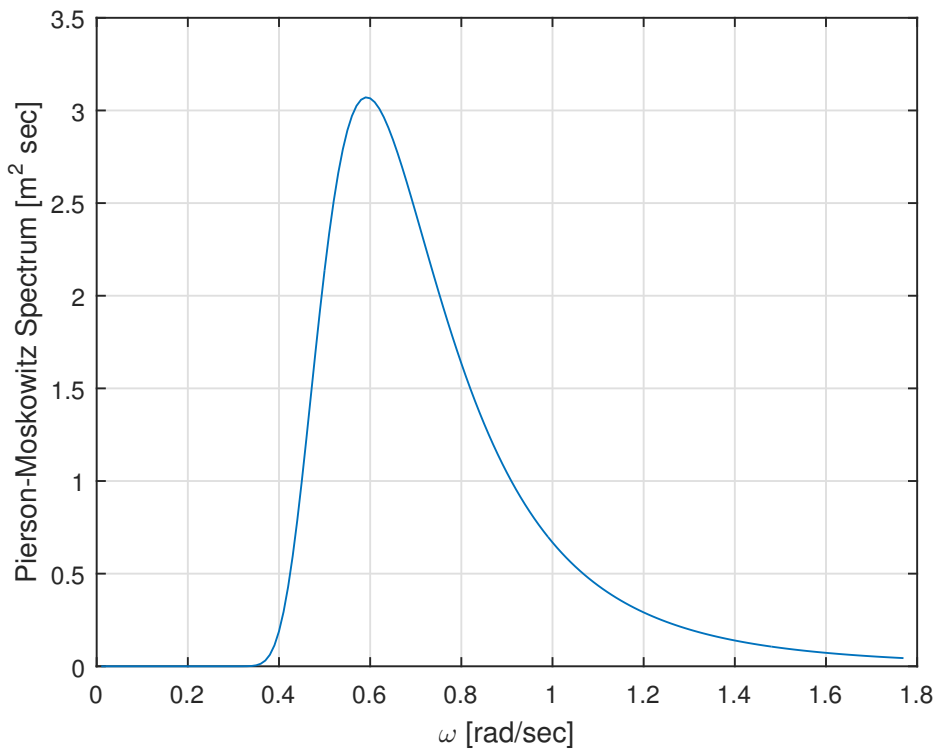
Figure 2.5: *Pierson-Moskowitz* spectrum

2.6 Wave Kinematic

The wave elevation is defined as in [23], namely:

$$\zeta(t,X,Y) = \frac{1}{2\pi} \int_{-\infty}^{\infty} W(\omega)\sqrt{2\pi S_\zeta^{2-sided}(\omega)}e^{-jk(\omega)[X\cos\xi + Y\sin\xi]}e^{j\omega t}d\omega \quad (2.16)$$

In the inertial reference frame, (X,Y) are the coordinates of a general point belonging to the SWL plane, ξ is the wave-propagation direction, $k(\omega)$ is the wave number and $W(\omega)$ is the Fourier transform of a White Gaussian noise (WGN) time-series process, characterized by a mean value $E[W] = 0$ and a variance $\sigma_W = 1$.

For water depth h, the wave number is correlated to the incident wave frequency, ω, and the gravitational acceleration constant g, as:

$$k(\omega)\tanh\left(k(\omega)h\right) = \frac{\omega^2}{g} \quad (2.17)$$

Solving the eq. (2.17) could result difficult. However considering the deep water hypothesis:

$$\frac{h}{\lambda} > \frac{1}{2} \quad (2.18)$$

where λ is the wavelength, it is possible to assume a simpler form:

$$k(\omega) = \frac{\omega^2}{g} \quad (2.19)$$

$S_\zeta^{2-sided}$ is the two-sided power spectral density of wave elevation per unit time. It is defined as:

$$S_\zeta^{\text{2-Sided}}(\omega) = \begin{cases} \frac{1}{2}S_\zeta^{\text{1-Sided}}(\omega) & for\,\omega \geq 0, \\ \frac{1}{2}S_\zeta^{\text{1-Sided}}(-\omega) & for\,\omega < 0 \end{cases} \quad (2.20)$$
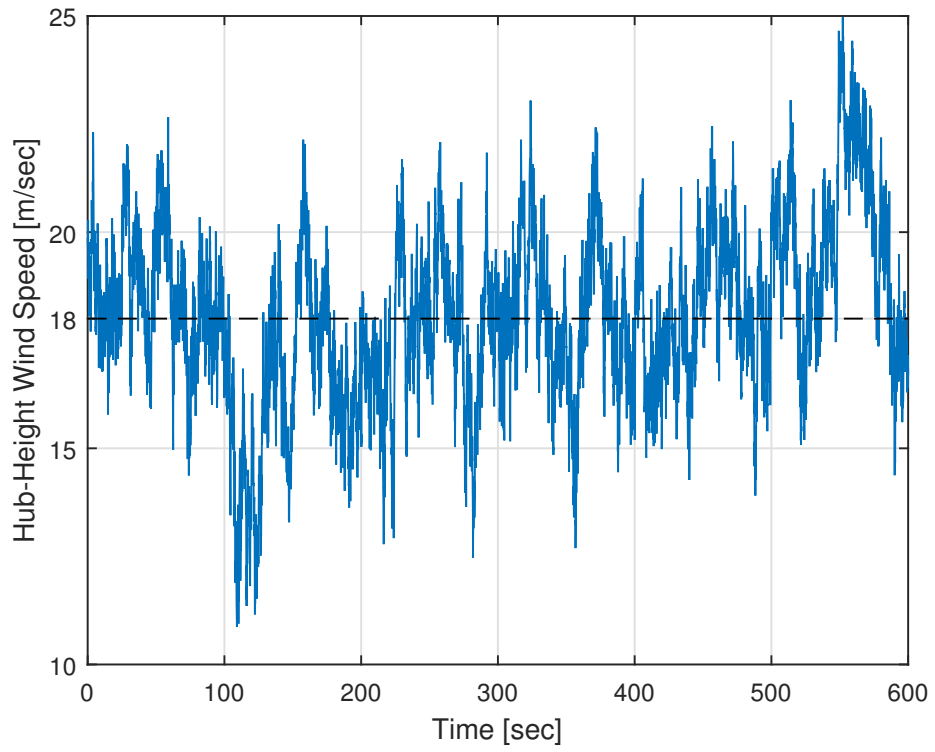
Figure 2.6: Wind Speed Time Series
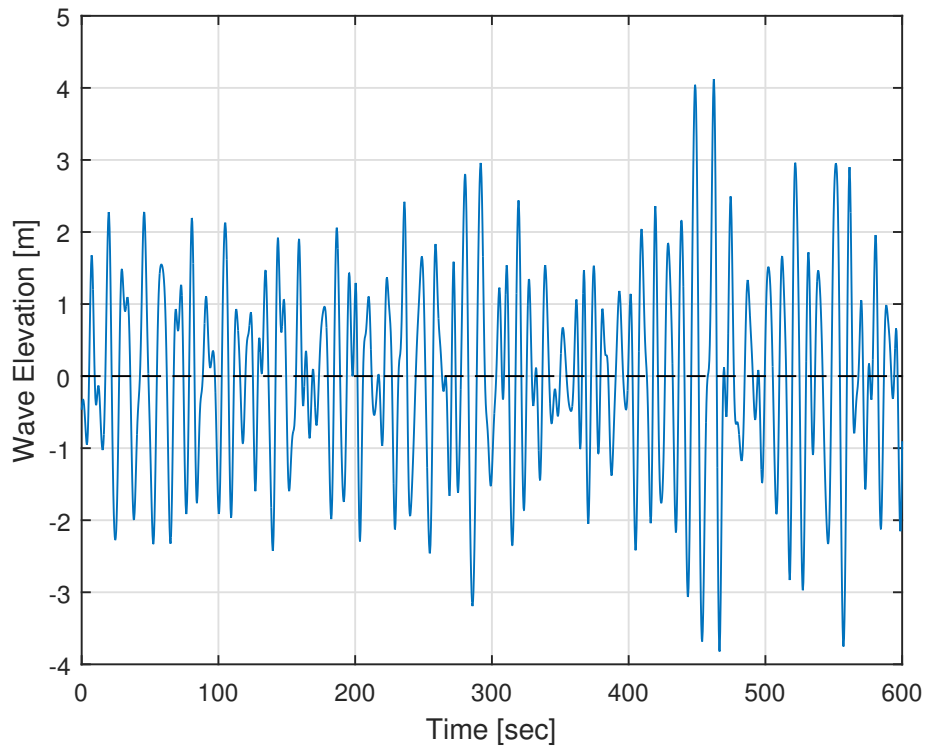
Figure 2.7: Wave Elevation Time Series

Chapter 3

Hydrodynamic Model

Shallow-water fixed-bottom offshore or onshore turbine loads are mainly dominated by aerodynamics. For offshore deepwater floating turbines, hydrodynamics loads become more important. The significance of hydrodynamics loads depends on the particular floating concept as well as on the wind severity and wave conditions, namely wind-speed, wave height and wave period. To compute the total hydrodynamics loads, *HydroDyn* [20], a NREL software coupled within *FAST*, has been used.

3.1 Floating Platform Structural Properties

The tower is cantilevered at a height of 10 meters above the SWL at the top of the floating platform. The latter, as defined in [22], has been considered a rigid body and the platform draft length has been evaluated equal to 120 meters. The OC3-Hywind spar-buoy consists in two cylindrical regions connected by a linear tapered conical region. The cylinder diameter is 6.5 meters above the taper and 9.4 meters below. In this way the hydrodynamics loads near the free surface are reduced.
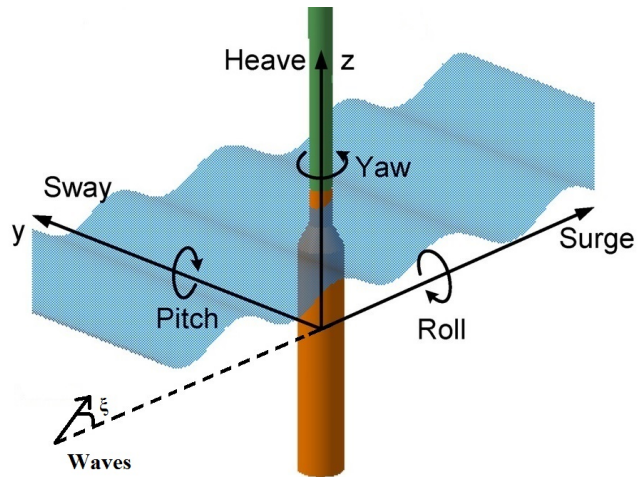
Figure 3.1: The Support Platform Degrees of Freedom

Figure 3.1 shows the support platform DOFs while table 3.1 summarizes the platform structural properties.

Parameter	Value	Unit
Total Drift	120	m
Tower Base Elevation	10	m
Depth to top of Taper below SWL	4	m
Depth to bottom of Taper below SWL	12	m
Platform Diameter above Taper	6.5	m
Platform Diameter below Taper	9.4	m
Platform Mass, Including Ballast	7466330	kg
CM Location below SWL	89.91	m
Platform Roll inertia about CM	4229230000	$kg\,m^2$
Platform Pitch inertia about CM	4229230000	$kg\,m^2$
Platform Yaw inertia about CM	164230000	$kg\,m^2$

Table 3.1: Floating Platform Structural Properties

3.2 Support Platform Loads

The overall loads of the support platform can be expressed as:

$$F_i^{\text{Platform}} = -A_{ij}\ddot{q}_{ij} + F_i^{\text{HydroDyn}} + F_i^{\text{Lines}} \qquad \text{with} \quad i = 1, ..., 6 \qquad (3.1)$$

where F_i^{Lines} is the ith component of the applied load on the support platform coming from the contribution of all mooring lines, A_{ij} is the impulsive hydrodynamic-added-mass matrix and F_i^{HydroDyn} is the ith component of the applied hydrodynamic load on the support platform. In eq. (3.1) i and j indicate the support platform DOFs (1=Surge, 2=Sway, 3=Heave, 4=Roll, 5=Pitch, 6=Yaw).

Einstein notation is used. In this equation as well in all the others reported in this chapter. Such a notation implies that, when the same subscript appears in multiple variables in a single term, there is a sum of all the possible terms.

3.2.1 Hydrodynamics Forces

The following formulation has been implemented to calculate hydrodynamic forces:

$$F_i^{\text{HydroDyn}} = F_i^{\text{Waves}} + F_i^{\text{Buoyancy}} + F_i^{\text{Radiation}} + F_i^{\text{Viscous}} + F_i^{\text{AddDamping}} \qquad (3.2)$$

where F_i^{Waves}, the total excitation load from incidents waves, is closely related to the wave elevation, ζ provided in eq. (2.16), F_i^{Buoyancy} is the total load contribution from hydrostatic, $F_i^{\text{Radiation}}$, the load contribution from the wave-radiation damping represents an additional contribution from added-mass that is not accounted for in A_{ij}, F_i^{Viscous} is the contribution of the total viscous-drag load and $F_i^{\text{AddDamping}}$ is the additional load contribution that captures all the hydrodynamic damping for the motion of the real *OC3-Hywind* platform.

The generic formulation of the hydrodynamic loads (incident wave and out-going wave radiation) depends on the flow separation occurrence. For a floating

platform interacting with surface waves, different formulation are applied to separated and not separated flows. For cylinders, the fitting formulation depends on the *Keulegan-Carpenter* number, K and on the oscillatory *Reynolds* number, Re, defined in [22] as:

$$K = \frac{VT}{D} \tag{3.3}$$

and

$$Re = \frac{VD}{\nu} \tag{3.4}$$

where ν is the kinematic viscosity of the fluid, V is the amplitude of the fluid velocity normal to the cylinder, T is the wave period and D is the cylinder diameter. The latter, as explained above, is not constant but changes according to the draft length, as indicated in following equation:

$$D(Z) = \begin{cases} 6.5 & |Z| < 4 \\ 9.4 & |Z| > 12 \\ 6.5 + 2|Z|\tan(\epsilon) & otherwise \end{cases} \tag{3.5}$$

where, $D(Z)$ is expressed in meters (m), $|Z|$ is the magnitude depth and ϵ is the angle formed between the oblique and shorter side of the isosceles trapezoid. In this study, the $D(Z)$ function has been calculated considering the cross section of the spar conical region, on the xz plane. The amplitude of the normal fluid velocity, V, has been derived a function of the wave height, H, and of the wave period, T. Hence:

$$V = \frac{\pi H}{T} \frac{\cosh\left[k(Z+h)\right]}{\sinh\left(kh\right)} \tag{3.6}$$

where k is the wave number, defined in eq. (2.19) and h is the water depth. Another important coefficient is the D/λ ratio, where λ is the wavelength defined as:

$$\lambda = \frac{2\pi}{k} \tag{3.7}$$

As shown in fig. (3.2a) and fig. (3.2b), the *Keulegan-Carpenter* (K) and oscillatory *Reynolds* numbers (Re) decrease according to depth along the spar, whereas D/λ ratio, in fig. (3.2c), is nearly constant along the spar except for the tapered region where it appears lower. As defined in [22], flow separation occurs when Keulegan-Carpenter number exceeds 2. For values lower than 2, potential flow theory can be applied. In this case, K results bigger than 2 only for a little portion of spar that is located above the tapered region. Diffraction effect is important when D/λ exceeds 0.2 and is unimportant for smaller ratios. In this case, D/λ is always lower than 0.2, hence the diffraction effect will be small.

In view of the validity of the potential flow theory, it is possible to apply and solve the potential-flow problem using *WAMIT* computer program [7]. *WAMIT* uses a three-dimensional numerical-panel method in the frequency domain to solve the linearized potential flow hydrodynamic radiation and diffraction problems for the interaction of surface waves with offshore platform of arbitrary geometry.
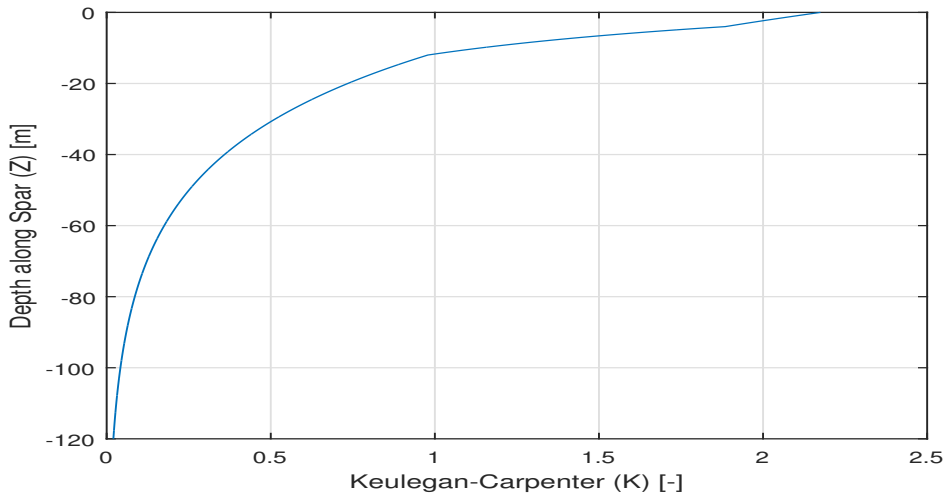
(a)
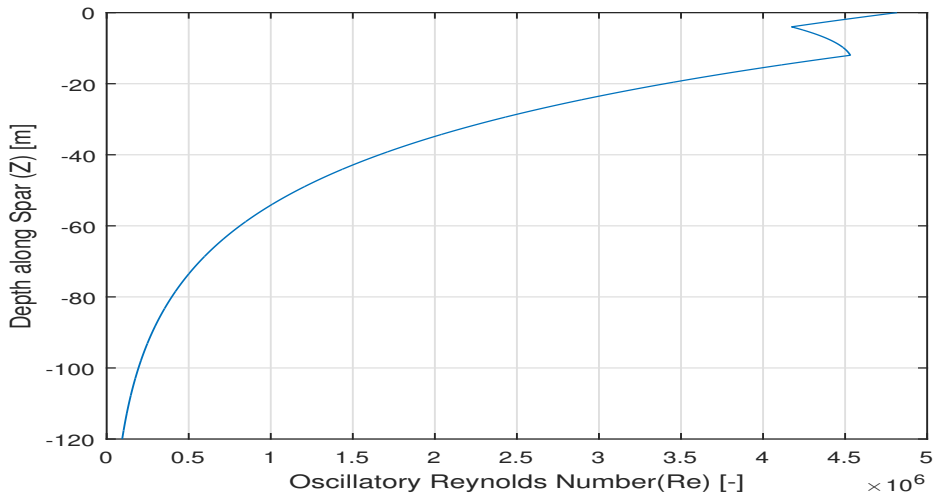
(b)
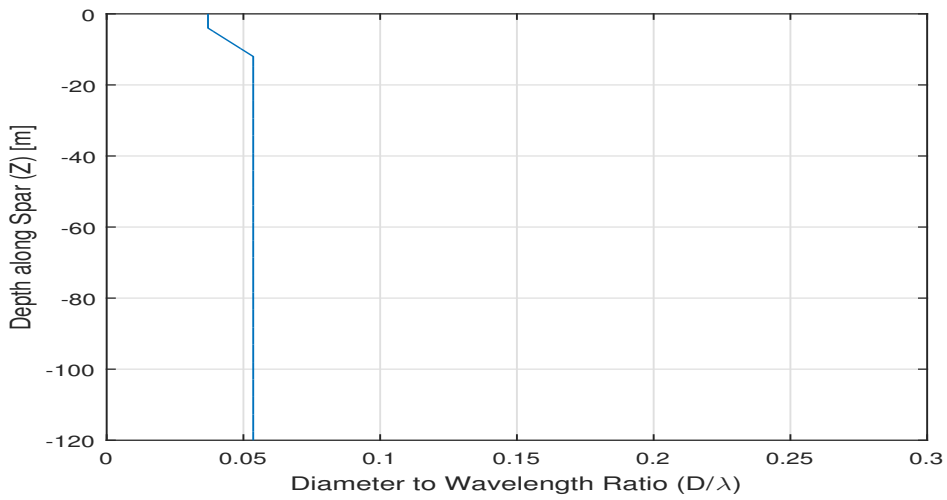
(c)

Figure 3.2: Dimensionless parameter with T and H defined in Tab. 2.2

3.3 The True Linear Hydrodynamic Model in the Time Domain

The true linear hydrodynamic model is useful for transient analysis when optional nonlinear effect and irregular wave formulation are introduced. The hydrodynamic problem can be split into three separate and simpler problems:

- Hydrostatic problem

- Diffraction problem

- Radiation problem

3.3.1 Hydrostatic Problem

The total load on the floating platform from linear hydrostatic is defined as:

$$F_i^{\text{Buoyancy}} = \rho g V_0 \delta_{i3} - C_{ij}^{\text{Hydro}} q_j \tag{3.8}$$

where ρ is the water density, g is the gravitational acceleration constant, V_0 is the displaced volume of the fluid when the support platform is in its undisplaced position, δ_{i3} is the $(i,3)$ component of the Kronecker-Delta function, C_{ij}^{Hydro} is the linear hydrostatic-restoring matrix of the incident and outgoing wave from diffraction and radiation problems and the q_j coefficient is the jth support platform DOF.

The first term in eq. (3.8) represents the buoyancy force from Archimedes' principle, namely the vertical force directed upward and equal to the weight of the displaced fluid, when the support platform is in its undisplaced position. This term is different from zero only for the vertical heave-displacement DOF of the support platform ($DOF\,i = 3$).

The second term in eq. (3.8) represents the variations in the hydrodynamic force and moment. These changes are caused by the effects of the water-plane area and by the COB (Center of Buoyancy), when the support platform is displaced. C_{ij}^{Hydro} matrix is formed by the following coefficients:

$$\begin{bmatrix} 0 & 0 & 0 & 0 & 0 & 0 \\ 0 & 0 & 0 & 0 & 0 & 0 \\ 0 & 0 & \rho g A_0 & 0 & -\rho g \iint_{A_0} x\, dA & 0 \\ 0 & 0 & 0 & \rho g \iint_{A_0} y^2\, dA + \rho g V_0 z_{\text{COB}} & 0 & 0 \\ 0 & 0 & -\rho g \iint_{A_0} x\, dA & 0 & \rho g \iint_{A_0} x^2\, dA + \rho g V_0 z_{\text{COB}} & 0 \\ 0 & 0 & 0 & 0 & 0 & 0 \end{bmatrix} \tag{3.9}$$

3.3.2 Diffraction Problem

The solution to the diffraction problem, which considers the hydrodynamic loads on the platform associated with excitation from incident wave, is given in terms of the wave-frequency and direction-dependent vector. This vector,

taken from *WAMIT*, is a complex vector whose magnitude is normalized per unit wave amplitude, water density and gravitational acceleration constant. The vector phase determines the lag between the wave elevation loads. Defined in [22] and shown in (3.3), the magnitude and the phase of the hydrodynamic-wave-excitation vector have been derived as functions of wave-frequency for the incident-waves propagated along the positive X-axis, namely with null wave direction, $\xi = 0$ deg. For these waves, the loads in direction of sway, roll and yaw are equal to zero because of the spar symmetries. The force magnitude of the surge DOF reaches a peak just above a wave frequency of $0.5\,rad/sec$, while the moment magnitude of the pitch DOF reaches a peak just below the same frequency. The heave force changes sign at about $0.25\,rad/sec$ and reaches a peak at $0.5\,rad/sec$. It is possible to observe that at a higher wave frequency, over $1.145\,rad/sec$, diffraction effects become important and loads drop.
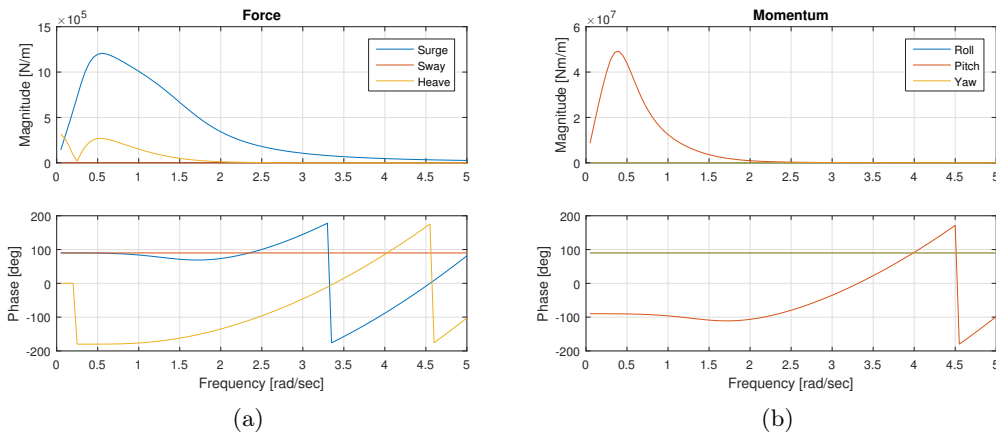
Figure 3.3: Hydrodynamic wave excitation per unit amplitude

The diffraction loads, F_i^{Waves} in eq. (3.2), are expressed as:

$$F_i^{\text{Waves}}(t) = \frac{1}{2\pi} \int_{-\infty}^{\infty} W(\omega)\sqrt{2\pi S_\zeta^{\text{2-Sided}}(\omega)} X_i(\omega, \xi) e^{j\omega t}\, d\omega \qquad (3.10)$$

Such relationship is closely related with the wave elevation ζ reported in eq. (2.16). The X_i term, extrapolated vector from *WAMIT*, represents the normalized load factor due to the incident waves. In this equation the wave elevation has been evaluated at the mean position of the support platform.

3.3.3 Radiation Problem

The solution to the radiation problem considers the hydrodynamic loads on the platform associated with oscillation of the platform in its various modes of motion. The hydrodynamic loads are given in terms of oscillatory-frequency dependent on hydrodynamic added-mass matrix, $A_{ij}(\omega)$, and hydrodynamic damping matrix, $B_{ij}(\omega)$, respectively. Unlike the X_i term, the coefficients are normalized per water density and frequency. As defined in [22], these matrices from the linear radiation problem are shown in fig. (3.4) as function of the oscillation frequency. Because of the $A_{ij}(\omega)$ and $B_{ij}(\omega)$ symmetries,

only the upper triangular matrix elements are shown. Moreover, due to the spar's symmetries, $\forall \omega$: $A_{11} = A_{22}$ and $B_{11} = B_{22}$ and likewise $A_{44} = A_{55}$ and $B_{44} = B_{55}$. The other matrix elements, not shown, are zero-valued.

As shown in figs. (3.4a), (3.4c) and (3.4e) the added-mass coefficient varies little across the frequency. Moreover, the values of the damping in the moment-rotation (fig. (3.4d)), force-rotation and moment-translational modes (fig. (3.4f)), emerge smaller than added-mass modes. This implies that also the linear radiation damping and the associated memory effect in the time domain are small in those modes. However, the contribution to the force-translational modes, shown in fig. (3.4b), can not be neglected.

In eq. (3.1), the impulsive hydrodynamic-added-mass components, A_{ij}, represent, as in [23], a force mechanism proportional to the acceleration of the support platform in the time-domain radiation problem. It is defined as:

$$A_{ij} = \lim_{\omega \to \infty} A_{ij}(\omega) = A_{ij}(\infty) \tag{3.11}$$

where the (i, j) component indicates the hydrodynamic force in direction of $i - DOF$. It results from the integration (over the wetter surface of the support platform) of the component of the outgoing-wave pressure field. This one is inducted by a unit acceleration of the jth–DOF of the support platform. The A_{ij} matrix in eq. (3.11) does not consider the memory effect that is captured from a integral of convolution representing the load contribution from wave-radiation damping, defined as:

$$F_i^{\text{Radiation}}(t) = -\int_0^t Kij(t - \tau)\dot{q}_j(\tau)\, d\tau \tag{3.12}$$

where, τ is a dummy variable with the same units as the simulation time, t. K_{ij}, defined in eq. (3.13), represents the radiation-retardation kernel, which has been obtained applying Fourier-transform at $B_{ij}(\omega)$.

$$K_{ij}(t) = \frac{2}{\pi} \int_0^\infty B_{ij}(\omega) \cos(\omega t)\, d\omega \tag{3.13}$$
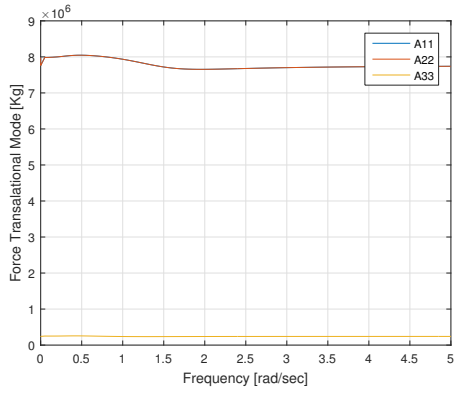
(a)
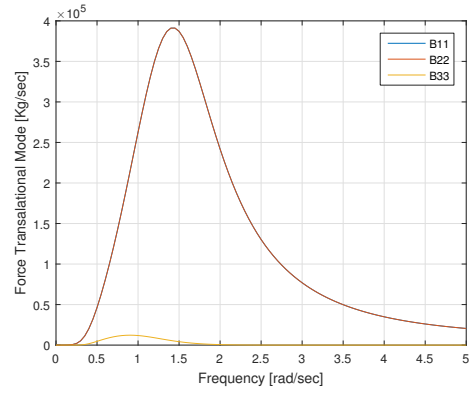
(b)
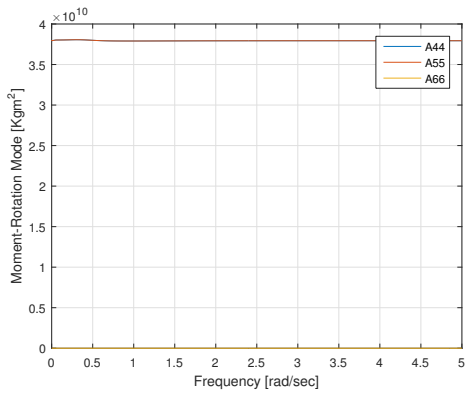
(c)
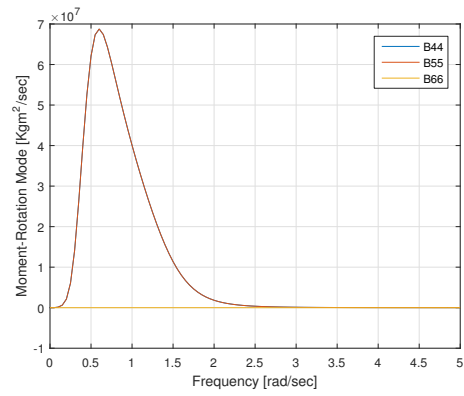
(d)
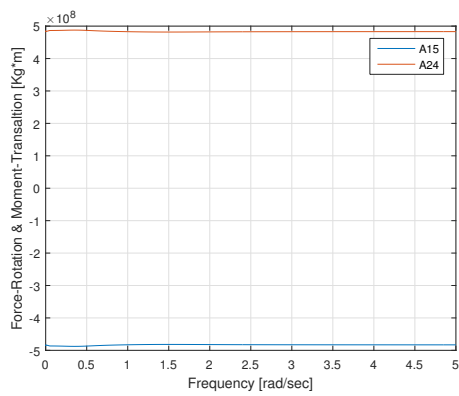
(e)
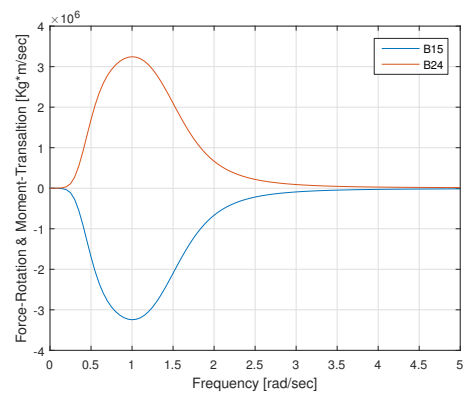
(f)

Figure 3.4: Hydrodynamic–added–mass and –damping

3.4 Morison's Equation

In severe sea conditions, the hydrodynamic loads formulation from linear potential-flow must be augmented with the loads brought about by flow separation. The most famous hydrodynamic formulation adopted for offshore wind turbines is the Morison's formulation. Morison's equation is applicable for the calculation of the hydrodynamic loads on cylindrical structures when:

1. The effects of diffraction are negligible

2. Radiation damping is negligible

3. Flow separation may occur

In this model a mixed formulation, namely the Morison's equation, has been used only for viscous forces applied along the portion of the spar, l, where flow separation occurs. The total contribution from viscous-drag load is represented as:

$$F_i^{\text{Viscous}}(t) = \int_l dF_i^{\text{Viscous}}(t,z)\,dz \tag{3.14}$$

where the contribution along surge, sway and heave is defined as reported in eq. (3.15):

$$dF_i^{\text{Viscous}}(t,z) = \begin{cases} \frac{1}{2}C_D\rho(Ddz)[v_i(t,0,0,z) - \dot{q}_i]|v(t,0,0,z) - \dot{q}(z)| & \text{for } i\text{=1, 2} \\ 0 & \text{for } i\text{=3} \end{cases} \tag{3.15}$$

where C_D is the normalized viscous-drag coefficient, v_i is the component of the undisturbed fluid particle velocity in the direction of $i-DOF$ and (Ddz) is the frontal area for the cylinder strip, where dz is the length of the differential strip and D is the diameter of the cylinder.

A similar expression can be written for roll, pitch and yaw moments:

$$dF_i^{\text{Viscous}}(t,z) = \begin{cases} -dF_2^{\text{Viscous}}(t,z)z & for\ i = 4 \\ dF_1^{\text{Viscous}}(t,z)z & for\ i = 5 \\ 0 & for\ i = 6 \end{cases} \tag{3.16}$$

The undisturbed fluid-particle acceleration and velocity in the direction of DOF-i, a_i and v_i respectively, at point (X,Y,Z) in the inertia reference frame are:

$$v_1(t,X,Y,Z) = \frac{\cos\phi}{2\pi}\int_{-\infty}^{\infty} W(\omega)\sqrt{2\pi S_\zeta^{\text{2-Sided}}(\omega)}e^{-jk(\omega)[X\cos\phi+Y\sin\phi]}\,\omega\,\Pi\,d\omega \tag{3.17}$$

$$v_2(t,X,Y,Z) = \frac{\sin\phi}{2\pi}\int_{-\infty}^{\infty} W(\omega)\sqrt{2\pi S_\zeta^{\text{2-Sided}}(\omega)}e^{-jk(\omega)[X\cos\phi+Y\sin\phi]}\,\omega\,\Pi\,d\omega \tag{3.18}$$

and

$$a_1(t, X, Y, Z) = \frac{j \cos \phi}{2\pi} \int_{-\infty}^{\infty} W(\omega) \sqrt{2\pi S_\zeta^{\text{2-Sided}}(\omega)} e^{-jk(\omega)[X \cos \phi + Y \sin \phi]} \omega^2 \, \Pi \, d\omega$$
(3.19)

$$a_2(t, X, Y, Z) = \frac{j \sin \phi}{2\pi} \int_{-\infty}^{\infty} W(\omega) \sqrt{2\pi S_\zeta^{\text{2-Sided}}(\omega)} e^{-jk(\omega)[X \cos \phi + Y \sin \phi]} \omega^2 \, \Pi \, d\omega$$
(3.20)

where Π relationship has been reported below due to a graphic issue. It is defined as:

$$\Pi = \frac{\cosh[k(\omega)(Z + h)]}{\sinh[k(\omega)h]} e^{j\omega t}$$
(3.21)

Morison's representation assumes that viscous drag prevails on the damping. This assumption implies that wave-radiation can be ignored. Indeed, the viscous-drag load is not part of the linear hydrodynamic loading equation since the viscous-drag load is proportional to the square of the velocity between the fluid particles and the platform.

3.5 Additional Damping

The linear radiation damping resulting from potential-flow theory, and the non linear viscous-drag, derived from the relative Morison's formulation, when added up do not capture all of the hydrodynamic damping for the motions of a real *Hywind* platform. For this reason, this support needs to be augmented as indicated in [22] with an additional linear damping. This is defined as:

$$F_i^{\text{AddDamping}}(\dot{q}) = B_{ij}^{\text{Linear}} \dot{q}_j$$
(3.22)

with

$$B_{ij}^{\text{Linear}} = \begin{bmatrix} 10^5 \frac{N}{m/s} & 0 & 0 & 0 & 0 & 0 \\ 0 & 10^5 \frac{N}{m/s} & 0 & 0 & 0 & 0 \\ 0 & 0 & 13 * 10^4 \frac{N}{m/s} & 0 & 0 & 0 \\ 0 & 0 & 0 & 0 & 0 & 0 \\ 0 & 0 & 0 & 0 & 0 & 0 \\ 0 & 0 & 0 & 0 & 0 & 13 * 10^6 \frac{Nm}{rad/s} \end{bmatrix}$$
(3.23)

where B_{ij}^{Linear} is the additional linear damping matrix and $\dot{q}_j$ is the first time derivative of the jth platform DOF.

The second order potential flow solution that includes mean-drift, slow-drift, and sum frequency solution excitation and higher order solution, have not been solved and have been presupposed to be negligible for the *OC3-Hywind* spar.

Table (3.2) summarizes the adopted hydrodynamic properties.

Parameter	Value	Unit
Water Density (ρ)	1025	kg/m^3
Water Depth (h)	320	m
Buoyancy Force in undisplaced position ($\rho g V_0$)	80708100	N
Hydrostatic Restoring in Heave ($C_{33}^{\text{Hydrostatic}}$)	332941	N/m
Hydrostatic Restoring in Roll ($C_{44}^{\text{Hydrostatic}}$)	-4999180000	Nm/rad
Hydrostatic Restoring in Pitch ($C_{55}^{\text{Hydrostatic}}$)	-4999180000	Nm/rad
Viscous-Drag Coefficient (C_D)	0.6	$-$
Additional Linear Damping in Surge (B_{11}^{Linear})	100000	$N/(m/sec)$
Additional Linear Damping in Sway (B_{22}^{Linear})	100000	$N/(m/sec)$
Additional Linear Damping in Heave (B_{33}^{Linear})	130000	$N/(m/sec)$
Additional Linear Damping in Surge (B_{66}^{Linear})	13000000	$Nm/(rad/sec)$

Table 3.2: Floating Platform Hydrodynamic Properties

3.6 Mooring Line

The Hywind platform is moored by a system of three catenary lines. It prevents the platform drift. A mooring system is made up of a number of cables attached to the floating support platform at fairlead connections with the opposite ends anchored to the seabed. Restraining forces at the fairlead are established through tension in the mooring lines. This tension depends on: i) the support platform buoyancy, ii) the elasticity in the cable, iii) the cable weight in the water, iv) the geometrical layout of the mooring system and v) the effects of the viscous-separations. Lines are attached to the platform through a delta connection to increase the mooring yaw.

In order to simplify the analysis of the mooring system, as in [22], three simplifications have been taken into account:

- Delta connection has been eliminated. This requires that the mooring system has to be augmented with a yaw spring to achieve the proper overall yaw stiffness.

- Multi-segment lines have been replaced with an equivalent homogeneous line, whose proprieties have been derived as the average weight values of the mass, weight and stiffness.

- All mooring system damping, including the hydrodynamic drag and line-to-seabed drag, has been neglected.

Table (3.3) summarizes mooring system properties considering the aforementioned simplifications.

If the mooring system agreement is essentially linear, mooring damping and inertia can be ignored. Therefore, the mooring lines contribute on the total load of the support platform, F_i^{Lines}, from eq. (3.1), is:

$$F_i^{\text{Lines}} = F_i^{\text{Lines},0} - C_{ij}^{\text{Lines}} q_j \tag{3.24}$$

Parameter	Value	Unit
Number of Mooring Lines	3	−
Angle Between Adjacent Lines	120	deg
Depth to Anchors Below SWL (Water Depth)	320	m
Depth to Fairleads Below SWL	70	m
Radius to Anchors from Platform Centreline	853.87	m
Radius to Fairleads from Platform Centreline	5.2	m
Unstretched Mooring Line Length	902.2	m
Mooring Line Diameter	0.09	m
Equivalent Mooring Line Mass Density	77.7066	kg/m
Equivalent Mooring Line Weight in Water	698.094	N/m
Equivalent Mooring Line Extensional Stiffness	384243000	N
Additional Yaw Spring Spring Stiffness	98340000	Nm/rad

Table 3.3: Mooring System Properties

where, the first term, $F_i^{\text{Lines},0}$, is the ith component of the total mooring system load acting on the support platform in its undisplaced position and C_{ij}^{Lines} is the (i, j) component of the linearized restoring matrix from all mooring lines. For catenary mooring lines, $F_i^{\text{Lines},0}$ represents the pretension at the fairleads from the cable weight not resting on the sea-floor. Furthermore, it represents a taut mooring due to an excessing buoyancy of the tank, by including the cable weight contribution. If the buoyancy of the catenary lines were neutral, $F_i^{\text{Lines},0}$ would be zero. The second term, C_{ij}^{Lines}, is the combined result of the effective geometric stiffness and the mooring lines elastic stiffness, brought about by the cables weight and depending on the mooring system layout.

However, in general, the mooring system dynamics are not linear in nature, hence, to consider apparent weight in fluid, elastic stretching and seabed friction of each line, *FAST* uses a *quasi-static* module as like explain in [18].

In figure (3.5) a typical line is shown. A fairlead local frame is used to determine its location relative to the anchor, x_F and z_F respectively.
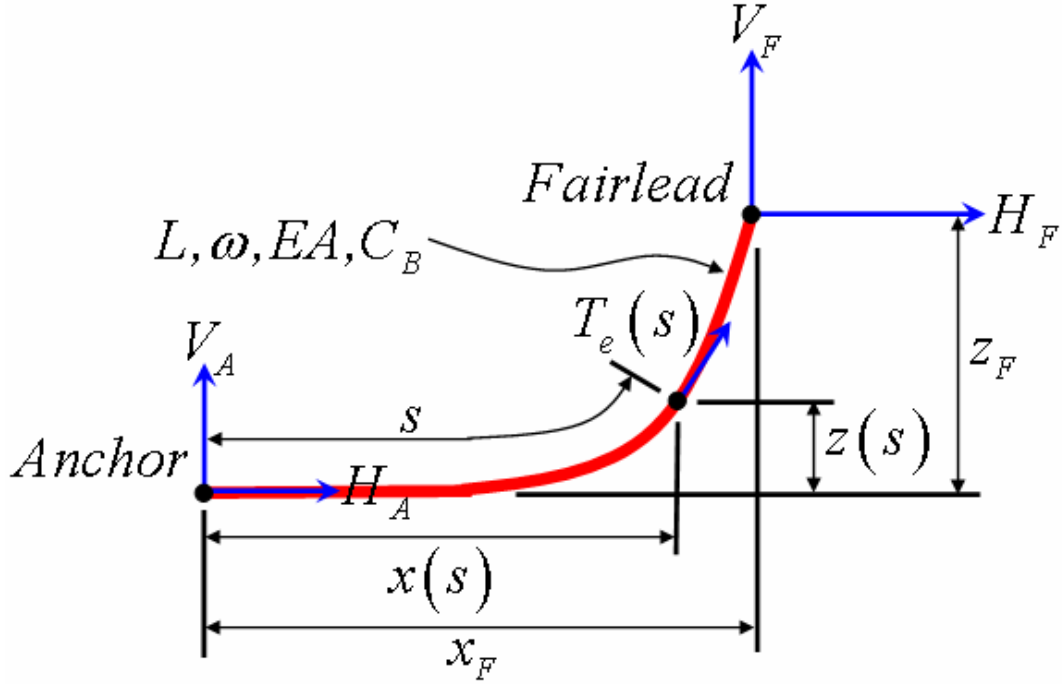
Figure 3.5: Single Mooring Line in xz local axis

In the local coordinate system, the analytical formulation is given in terms of a nonlinear equation in two unknowns, which are the vertical and horizontal components of the effective tension at the fairlead, V_F and H_F respectively.

The analytical formulation is as follow:

$$x_F(H_F, V_F) = L - \frac{V_F}{\upsilon} + \frac{H_F}{\upsilon} \ln\left[\frac{V_F}{H_F} + \sqrt{1 + \left(\frac{V_F}{H_F}\right)^2}\right] + \frac{H_F L}{EA}$$

$$+ \frac{C_B \upsilon}{2EA}\left[-\left(L - \frac{V_F}{\upsilon}\right)^2 + \left(L - \frac{V_F}{\Upsilon} - \frac{H_F}{C_B \upsilon}\right) \max\left(L - \frac{V_F}{\upsilon} - \frac{H_F}{C_B \upsilon}, 0\right)\right] \quad (3.25)$$

and

$$z_F(H_F, V_F) = \frac{H_F}{\upsilon}\left[\sqrt{1 + \left(\frac{V_F}{H_F}\right)^2} - \sqrt{1 + \left(\frac{V_F - \upsilon L}{H_F}\right)^2}\right] + \frac{1}{EA}\left(V_F L - \frac{\upsilon L^2}{2}\right)$$

$$(3.26)$$

where:

- EA is the cross-section axial stiffness

- L is the unstretched line length

- $\upsilon = gA(\rho_c - \rho)$ is the weight per unit length in the submerged fluid, where ρ_c is the cable density, ρ is the fluid density and g is the gravity acceleration

- C_B is the stretched portion of the mooring line resting on the seabed that is affected by static friction

26

The seabed friction has been modelled as a simply drag force per unit length of $C_B v$. It is important to note that the first two terms on the right-side of equation (3.25) represent the unstretched portion of the mooring line resting in the seabed, L_B:

$$L_B = L - \frac{V_F}{v} \tag{3.27}$$

If there is not a portion of the mooring line on the seabed, then $L_B = 0$. The *max*-function, in (3.25), is needed to handle cases with and without anchor tension. Specifically:

$$\max\left(L - \frac{V_F}{v} - \frac{H_F}{C_B v}, 0\right) \rightarrow \begin{cases} = 0 & if\ H_A \neq 0 \ \vee \ V_A \neq 0 \\ \neq 0 & if H_A = 0 \ \vee \ V_A = 0 \end{cases} \tag{3.28}$$

where H_A and V_A are the horizontal and vertical components of the effective tension at the anchor. Hence, *max*-function is equal to zero if the seabed friction is too weak to overcome the horizontal tension in the mooring line.

The mooring system module uses a Newton-Raphson iteration scheme to solve non-linear eqs. (3.25) and (3.26). Its implementation within FAST has been explicated in [18].

Once the effective tensions, H_F and V_F, have been found, the anchor tensions can be derived simply. Looking at fig. (3.5) from a balance of external forces, it can be verified that:

$$H_A = \max\left(H_F - C_B v L_B\right) \tag{3.29}$$

$$V_A = \begin{cases} V_F - vL, & \text{when line does not rest on the seabed} \\ 0, & \text{when line rests on the seabed} \end{cases} \tag{3.30}$$

The total load on the support from the contribution of all mooring lines, F_i^{Lines} from eq. (3.1) is calculated firstly by transforming each fairlead tension from its local mooring line coordinate system to the global frame and then summing up the tensions from all lines.

Chapter 4

Aerodynamic Loads

In this chapter the aerodynamic loads and the tower deflections are explained. The firsts have been developed using *AeroDyn* [8], a NREL software, which takes as input the wind model developed in chapter 2.1. The seconds do not need an external CAE but their modelization is integrated in FAST. For this reasons a brief description on how they are implemented is provided. Finally, a brief focus about the drivetrain model and the system actuators is reported.

4.1 Blade Element Momentum Theory

To calculate the effect of the wake on the turbine rotor aerodynamics the *blade element momentum theory* (BEMT) has been used. This theory, defined in [28], is one of the oldest and prevalent method implemented to calculate inducted velocities on wind turbines blades. It is an extension of the actuator disk theory [17] proposed by Rankine and Froude. The BEMT, generally attributed to Betz and Glauert, has its origin from two different theories:

- Blade Element Theory (BET)

- Momentum Theory (MT)

Both defined in [26].

Figure 4.1: Annular plane used in *BEMT*

The *Momentum Theory* (MT) assumes that the loss of pressure, or momentum, is caused by the work done by the airflow when it passes through the rotor plane. In other words, it considers the wake rotation effects.

The *Blade Element Theory* (BET) uses several annular stream tube control volumes. At the rotor plane, the boundaries of these control volumes split the

28

blade into a number of distinct elements, each long dr (fig. 4.1). Blade geometry and flow stream properties, at each element, can be related to a differential rotor torque, dQ, and to a differential rotor thrust, dT.

As stated in [24], the aforementioned connections can be applied in the BET only under the following assumptions:

- There is no interaction between the analysis of each blade element. In other words, every annular stream tube control volume is assumed without interactions.

- The forces exerted on the blade elements by the flow stream are determined by the two-dimensional lift and drug coefficients only. These are characteristics of the blade element airfoil shape and orientation relative to the incoming flow.

The differential rotor thrust and the differential rotor torque, acting on each blade element, can be found from a geometry analysis depicted in figure (4.2). As shown, the blade is specified as propagating to the left as a result of blade rotation. The contribution of the pitching moment is absent because it is null to the rotor torque and trust. In the same figure, β is the blade collective pitch angle and θ is the angle of the relative incoming flow stream with respect to the plane of rotation.
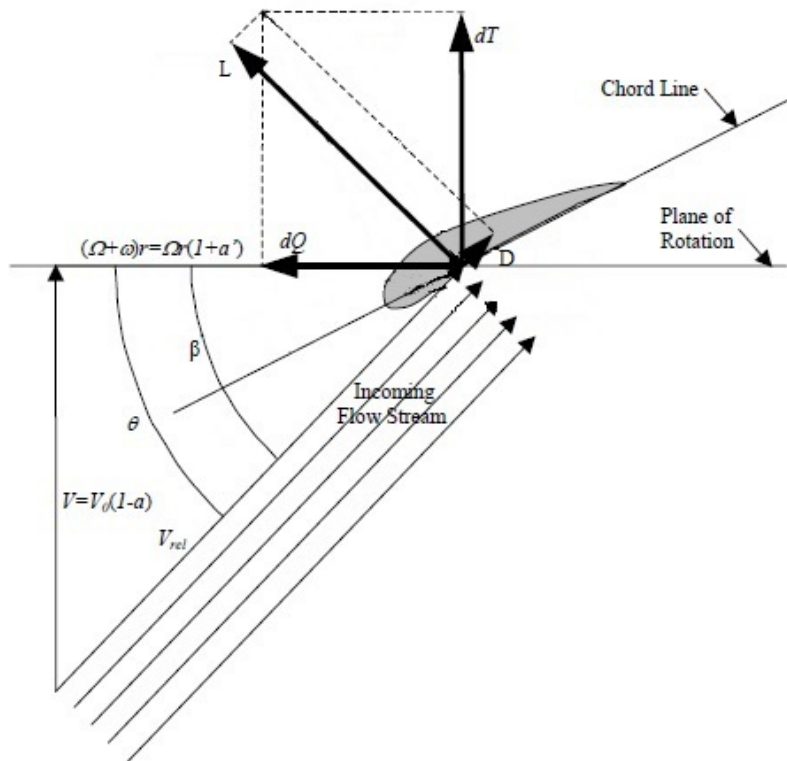
Figure 4.2: Blade Element Theory

From the analysis of the blade element geometry presented in figure (4.2), it is possible to achieve the following relationships:

$$dT = L\cos\theta + D\sin\theta \tag{4.1}$$

and

$$dQ = r[L\sin\theta - D\cos\theta] \tag{4.2}$$

where r is the local radius, L and D are the lift and drug forces, respectively.

To be more precise, the lift and the drug forces shown in fig. (4.2) and used in eqs. (4.1) and (4.2), represent the differential components of the forces given by the flow stream on the blade element, whose cross- section is shown. Moreover, all differential forces used in those equations are the differential forces action on a single blade. Hence, since the wind turbine has a $B = 3$ identical blades, the differential, dT, and the differential rotor torque, dQ, are equals to the following equations when substituting the dimensionless coefficients for the forces:

$$dT = B\frac{1}{2}\rho_{air}V_{rel}^2\big[C_L\cos\theta + C_D\sin\theta\big]c\,dr \tag{4.3}$$

and

$$dQ = B\frac{1}{2}\rho_{air}V_{rel}^2\big[C_L\cos\theta - C_D\sin\theta\big]c\,dr \tag{4.4}$$

where B is the number of blades, ρ_{air} is the air density, V_{rel} is the velocity of the incoming flow stream, C_L is the lift coefficient, C_D is the drug coefficient, c is the chord length and dr is the radius thickness.

In order to relate the inducted velocities in the rotor plane to the elemental forces of eqs. (4.3) and (4.4), the momentum part of the theory must be incorporated. According to [28], the thrust and the torque, extracted by each rotor annulus, are equivalent to:

$$dT = 4\pi r\rho_{air}V_0^2(1-a)a\,dr \tag{4.5}$$

$$dQ = 4\pi r^3\rho_{air}V_0\Omega(1-a)a'dr \tag{4.6}$$

where V_0 is the mean wind speed, Ω is the rotor rotational speed, a is the axial induction factor and a' is the rotational induction factor. In particular, the coefficient a is defined as:

$$a = \frac{V_0 - V}{V} \tag{4.7}$$

where V is the flow velocity through the rotor disc and $V_0 - V$ is the inducted velocity. The coefficient a' is defined as:

$$a' = \frac{1}{2}\left(\sqrt{1 + \frac{4}{\lambda_r^2}a(1-a)} - 1\right) \tag{4.8}$$

where λ_r is the local speed ratio, defined as:

$$\lambda_r = \frac{\Omega r}{V_0} \tag{4.9}$$

The previous equations do not include terms for coning angle of the rotor plane. This is because *AeroDyn* assumes that the aerodynamics of a rotor in operation do not change significantly.

One of the major limitations of the BEMT, is that there is no influence of vortices created from the blade extremity into the wake on the inducted velocity field. These vortices create multiple helical structures in the wake and have a great influence in the inducted velocity distribution in the rotor. These effects are most pronounced near the blade tips and the rotor hub. However, it is possible to compensate such deficiencies introducing the *Tip–Loss* and *Hub–Loss* Models.
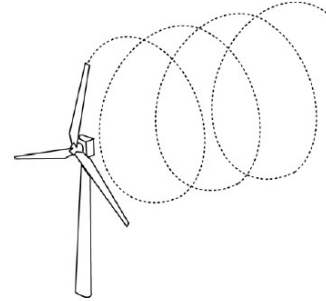
Figure 4.3: Helical Wake caused by tip-blade

4.1.1   Tip–Loss Model

Prandtl simplified the wake by modelling an helical vortex wake pattern to a convected vortex sheet by the mean flow and have no direct effect on the wake itself. This theory is summarized by the factor, F, defined as:

$$F_{tip} = \frac{2}{\pi} \cos^{-1} e^{-f_{tip}} \tag{4.10}$$

where,

$$f_{tip} = \frac{B}{2} \left(\frac{R - r}{r \sin \theta} \right) \tag{4.11}$$

4.1.2   Hub–Loss Model

Much like the *Tip–Loss Model*, the *Hub–Loss Model* can be used to correct the inducted velocity resulting from a vortex created near a rotor hub. In this case, the factor can be summarized as follows:

$$F_{hub} = \frac{2}{\pi} \cos^{-1} e^{-f_{hub}} \tag{4.12}$$

where,

$$f_{hub} = \frac{B}{2} \left(\frac{r - R_{hub}}{R_{hub} \sin \theta} \right) \tag{4.13}$$

where R_{hub} is the hub radius.

For a given element, the local aerodynamics may be affected by both the tip-loss and hub-loss, as represented in fig. (4.4). In this case the correction factors are multiplied to calculate the total loss factor:

$$F = F_{tip} F_{hub} \tag{4.14}$$
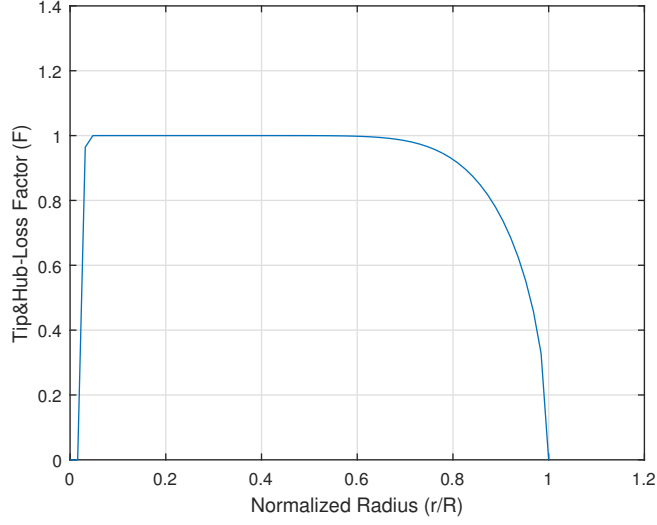
Figure 4.4: Tip-Loss and Hub-Loss Factor with constant $\theta = 10\,deg$

This correction factor is used to modify the momentum part of the blade element momentum equation, replacing eqs. (4.5) and (4.6) with the following:

$$dT = 4\pi r \rho V_0^2 (1-a)aF\,dr \qquad (4.15)$$

$$dQ = 4\pi r^2 \rho V_0 \Omega (1-a)a'F\,dr \qquad (4.16)$$

As soon as all the equations and corrections of $BEMT$ have been established, $AeroDyn$ [8] can identify the inducted velocities, the angles of attack and the thrust coefficients for each blade. The iterative procedure is not presented because it is not included in the scope of this thesis.

The power extracted from the wind by rotor, P_A, can be calculated as follows:

$$P_A = \int \Omega\,dQ \qquad (4.17)$$

where the product of the differential torque and the angular speed of the rotor represents the differential power extracted from the turbine, dP_A.

4.2   Drivetrain Model

The drivetrain is modelled as an equivalent shaft that separates the generator and the hub. The shaft is characterized by a linear torsional spring and a dumper, k_{ls} and c_{ls}, respectively. The equation governing the low-speed-shaft torque of the spring-damper is:

$$T_{ls} = k_{ls}(\Psi - \Upsilon) + c_{ls}(\dot{\Psi} - \dot{\Upsilon}) \qquad (4.18)$$

where Ψ is the rotor azimuth and Υ is the shaft angle entering in the gear box low–speed side.
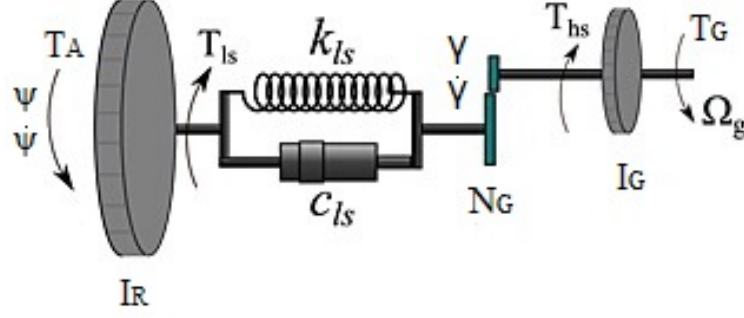
Figure 4.5: Two–mass drivetrain model

The driveshaft model is depicted in figure (4.5) and its properties are presented in table (4.1), according to the parameters chosen in [23], [18] and [22].

Parameter	Value	Unit
Rated Rotor Speed	12.1	rpm
Rated Generator Speed	1173.7	rpm
Gearbox Ratio (η_t)	97:1	$-$
Electrical Generator Efficiency	94.4	$\%$
Gearbox Efficiency	100.0	$\%$
Generator Inertia (HSS Side)	534,116	$kg\,m^2$
Equivalent Drive-Shaft Torsional-Spring Constant	867637000	Nm/rad
Equivalent Drive-Shaft Torsional-Damping Constant	6215000	$Nm/(rad/sec)$

Table 4.1: Drivetrain Properties

4.3   Tower Model and Deflections

The tower base is located at 10 meters of height above the still water level (SWL), coincident with the top of the platform. The tower top coincides with the yaw bearing, that is located at an elevation of 87.6 meters above the SWL.

Figure 4.6: Tower Bending

Defined in [24], [21] and implemented in FAST [19], the bottom part of the tower is modelled as rigid body until the height, H_S. As a consequence the length of the flexible part of the tower, H, is defined as:

$$H = H_H - \gamma - H_S \qquad (4.19)$$

where H_H is the hub elevation to the water's surface and γ is the vertical distance between the hub and the tower-top.
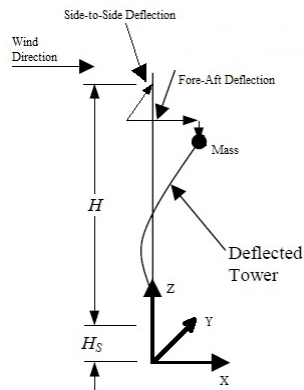
The tower is modelled as an inverted cantilever beam with a point of mass affixed to its free end. The point of mass represents the combined mass nacelle, hub and blades. The tower is assumed to deflect

33

in the longitudinal and lateral direction independently. The stiffness distribution is assumed identical in each direction. Consequently, the associated mode shapes and frequency are characterized by the same configuration in any direction.

In theory, as explicated in [24], these bodies are characterized by an infinite number of DOFs. In practice, they are modelled as a linear sum of known shapes of the dominant normal vibration modes. With the *Normal Mode Summation Method* it is possible to reduce the DOFs number from infinity to N.

Using the Lagrange's equation for a conservative system, the equations of motion for a N–DOFs system are equivalent to:

$$\sum_{j=p}^{N+p-1} m_{ij}\ddot{c}_j(t) + \sum_{j=p}^{N+p-1} k_{ij}c_j(t) = 0 \qquad i = p, p+1, \ldots, N+p-1 \quad (4.20)$$

where p is a parameter chosen for convenience ($p > 2$), c_j is the generalized coordinate, m_{ij} and k_{ij} are the generalized mass and stiffness, respectively. These last two terms are defined using the kinetics energy, T, and the potential energy, V:

$$T = \frac{1}{2} \sum_{i=p}^{N+p-1} \sum_{j=p}^{N+p-1} m_{ij}\dot{c}_i(t)\dot{c}_j(t) \qquad (4.21)$$

and

$$V = \frac{1}{2} \sum_{i=p}^{N+p-1} \sum_{j=p}^{N+p-1} k_{ij}c_i(t)c_j(t) \qquad (4.22)$$

The kinetic energy of the tower is characterized by two components. The first is associated with the distributed mass of the beam, while the second is looked through the point mass:

$$T = T_{beam} + T_{top} \qquad (4.23)$$

where the kinetic energy of a beam can be expressed:

$$T_{beam} = \frac{1}{2} \sum_{i=p}^{N+p-1} \sum_{j=p}^{N+p-1} \left(\int_0^H \mu_T(h)\phi_i(h)\phi_j(h)\,dh \right) \dot{c}_i(t)\dot{c}_j(t) \qquad (4.24)$$

where $\mu_T(h)$ is the distributed lineal density of the tower and $\phi_x(h)$ ($x = i$ or $x = j$) is the normal mode shape, that can be described by the following polynomial function:

$$\phi_x(h) = \left(\frac{h}{H} \right)^x \qquad (4.25)$$

Setting $\mu_T = M_{top}$ and considering ϕ_x evaluated at $h = H$, the kinetic energy of the affixed point mass reported in eq. (4.24) can be calculated as follows:

$$T_{top} = \frac{1}{2} \sum_{i=p}^{N+p-1} \sum_{j=p}^{N+p-1} \left(M_{top} \right) \dot{c}_i(t)\dot{c}_j(t) \qquad (4.26)$$

Equations (4.21), (4.22), (4.24) and (4.26) show that the generalized mass of the tower is:

$$m_{ij} = M_{top} + \int_0^H \mu_T(h)\phi_i(h)\phi_j(h)\,dh \tag{4.27}$$

According to eq. (4.28), the potential energy is characterized by two components; the first is related to the stiffness, while the second is associated with the gravity:

$$V = V_{beam} + V_{gravity} \tag{4.28}$$

In particular the potential energy can be expressed as:

$$V_{beam} = \frac{1}{2} \sum_{i=p}^{N+p-1} \sum_{j=p}^{N+p-1} \left(\int_0^H EI_T(h) \frac{d^2\phi_i(h)}{dh^2} \frac{d^2\phi_j(h)}{dh^2}\,dh \right) c_i(t)c_j(t) \tag{4.29}$$

where EI_T is the distributed stiffness of the tower.

Moreover, since the gravity action on an inverted beam tends to reduce the tower stiffness, it can be defined as:

$$V_{gravity} = -g\left[M_{top}\kappa(H,t) + \int_0^H \mu_T(h)\kappa(h,t)\,dh \right] \tag{4.30}$$

where the negative sign promotes the notation that gravity reduces the stiffness, $\kappa(h,t)$ is the axial deflection of the flexible cantilever beam at time t and an elevation h. The axial deflection is the combined result of two assumptions: i) the flexible beam remains fixed in length (measured along the beam's central axis) and ii) the free end can be moved closer to the fixed end when the beam deflects laterally. As a consequence, the axial deflection is related to the lateral deflection and their relationship can be obtained by examining the deflection geometry as shown in figure (4.7).
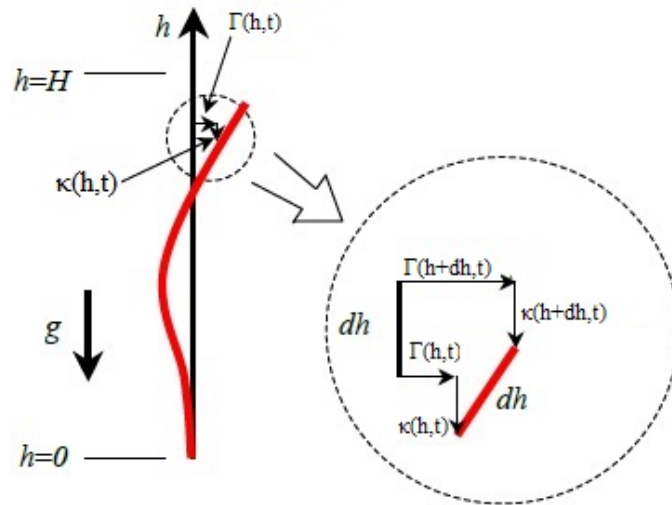
Figure 4.7: Tower deflection geometry

Expanding the lateral and the axial deflection about any h elevation, using a first Taylor series approximation, and applying the Pythagorean theorem to the geometry as stated in [24], it emerges that:

$$\kappa(h,t) = \frac{1}{2}\int_0^h \left[\frac{\partial\Gamma(h',t)}{\partial h'}\right]^2 dh' \tag{4.31}$$

where h' is a dummy variable representing the elevation along the flexible part of the tower. Therefore the equation (4.31) can be rewritten:

$$\kappa(h,t) = \frac{1}{2}\sum_{i=p}^{N+p-1}\sum_{j=p}^{N+p-1}\left(\int_0^h \frac{d\phi_i(h')}{dh'}\frac{d\phi_j(h')}{dh'}\,dh'\right)c_i(t)c_j(t) \tag{4.32}$$

Substituting eq. (4.32) into eq. (4.30), the potential energy caused by gravity can be expressed by the following formula:

$$\begin{aligned}
V_{gravity} = &-g\frac{1}{2}\sum_{i=p}^{N+p-1}\sum_{j=p}^{N+p-1}\left[M_{top}\int_0^H \frac{d\phi_i(h)}{dh}\frac{d\phi_j(h)}{dh}\,dh+\right.\\
&\left.\int_0^H \mu_T(h)\left(\int_0^h \frac{d\phi_i(h')}{dh'}\frac{d\phi_j(h')}{dh'}\,dh'\right)dh\right]c_i(t)c_j(t)
\end{aligned} \tag{4.33}$$

After some simplifications, equations (4.22), (4.28), (4.29) and (4.33) show that the generalized tower stiffness is:

$$\begin{aligned}
k_{ij} = &\int_0^H EI_T(h)\frac{d^2\phi_i(h)}{dh^2}\frac{d^2\phi_j(h)}{dh^2}dh\\
&-g\int_0^H \left[M_{top}+\int_h^H \mu_T(h')\,dh'\right]\frac{d\phi_i(h)}{dh}\frac{d\phi_j(h)}{dh}dh
\end{aligned} \tag{4.34}$$

Table (4.2) summarizes the undistributed tower properties.

Parameter	Value	Unit
Elevation to Tower Base Platform (above SWL)	10	m
Elevation to Tower Top (above SWL)	87.6	m
Overall (integrated) Tower Mass	249718	kg
Tower Top Mass (M_{top}) (rotor, nacelle and blades)	350000	kg
CM Location of Tower above SWL	43.3	m
Tower Structural-Damping Ratio (All Modes)	1%	$-$

Table 4.2: Undistributed Tower Properties

4.4   System Actuators

The system actuators are:

- The Electric Generator
- The Blade Pitch Actuator

4.4.1 Electric Generator

The wind turbines are usually variable-speed, where the rotor can rotate at variable frequencies independently of the electrical grid frequency. Using an electronic converter, it is possible to provide a variable rotational speed that allows achieving the maximum power in an ample wind speed range. Usually, the electric machine is an asynchronous motor controlled thought a vectorial controller, which produces rapid and precise torque variation. For these reasons, as in [3], the control system of the overall electric system can be approximated with a first order system characterised by a very small constant transfer. Moreover, since the generator dynamic is faster than the wind turbine mechanical dynamics, it is not taken into consideration.

4.4.2 Blade Pitch Actuator

The blades rotations allow to get the desired step angle, typically thought a servo-motor that can be electric or hydraulic. In the last years a servo-electric motor has been preferred because it is not influenced from the environmental conditions, since there is not fluid to move blades.

FAST can not model the system actuators. Since making an accurate model is useful for the purpose of this thesis, a second order transfer function with a natural frequency of 5.0265 rad/sec and dumping coefficient of 0.8, as in [3], has been used to model the blade pitch actuator.

Figure (4.8) shows the step response of the pitch blade actuator model.
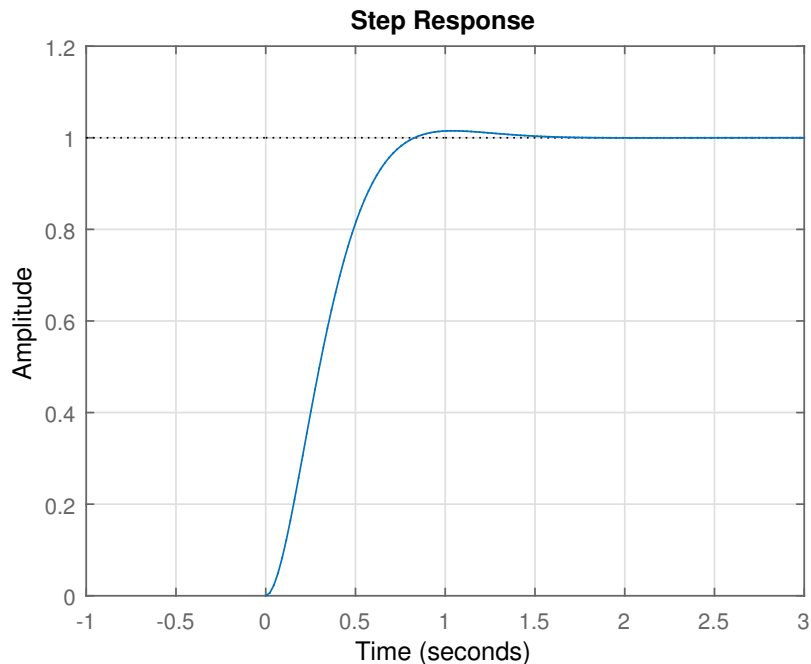
Figure 4.8: Blade Pitch Step Response

Chapter 5

Control Models

For the OC3–Hywind wind turbine a conventional variable-speed, defined in ([18], [23]), and a variable blade-pitch-to-father configuration have been used. The conventional approach for power production control and for mechanical stability relies on the design of two basic control systems:

- Generator–Torque Controller

- Full–Span Blade–Pitch Controller

The two control systems are designed to work independently, below and above the rated wind speed range. The objective of the Generator–Torque Controller is the power maximization below the rated operation point ($v_{\text{wind}} < 11.4$ m/sec), whereas the blade pitch controller has to regulate the generator speed above the rated operation point ($v_{\text{wind}} > 11.4$ m/sec) and below the cut-off region ($v_{\text{wind}} > 25$ m/sec). According to the purpose of this thesis, only the case above the rated operation point is considered.

5.1   Speed–Measurement Filter

Usually in multi-megawatt wind turbines, both generator-torque and blade pitch controllers have a generator speed measurement as feedback input. To mitigate the high-frequency excitation of the control system, a filtered generator speed has been used, as in [18]. The corner frequency of the low-pass filter was set to be roughly one-quarter of the blade first edgewise natural frequency (see table 6.1). The corner frequency will be 5.46 rad/s.

5.2   Generator–Torque Controller

The generator–torque controller is a tabulated function that incorporates five control regions as in [18]:

- Region 1 – Before cut-in wind speed, the generator torque is equal to zero and no electrical power is extracted. The wind energy is used to accelerate the rotor.

- Region $1\frac{1}{2}$ – Start-up region. It is a linear transition between regions 2 and 1.

- Region 2 – Optimizing power capture. Here, the generator torque is proportional to the square of the generator speed to maintain a constant (optimal) tip-speed ratio.

- Region $2\frac{1}{2}$ – Added region. This region is typically needed to limit tip speed (and noise emission) at a rated power.

- Region 3 – The generator power is held constant. Hence, the generator torque is inversely proportional to the generator speed.
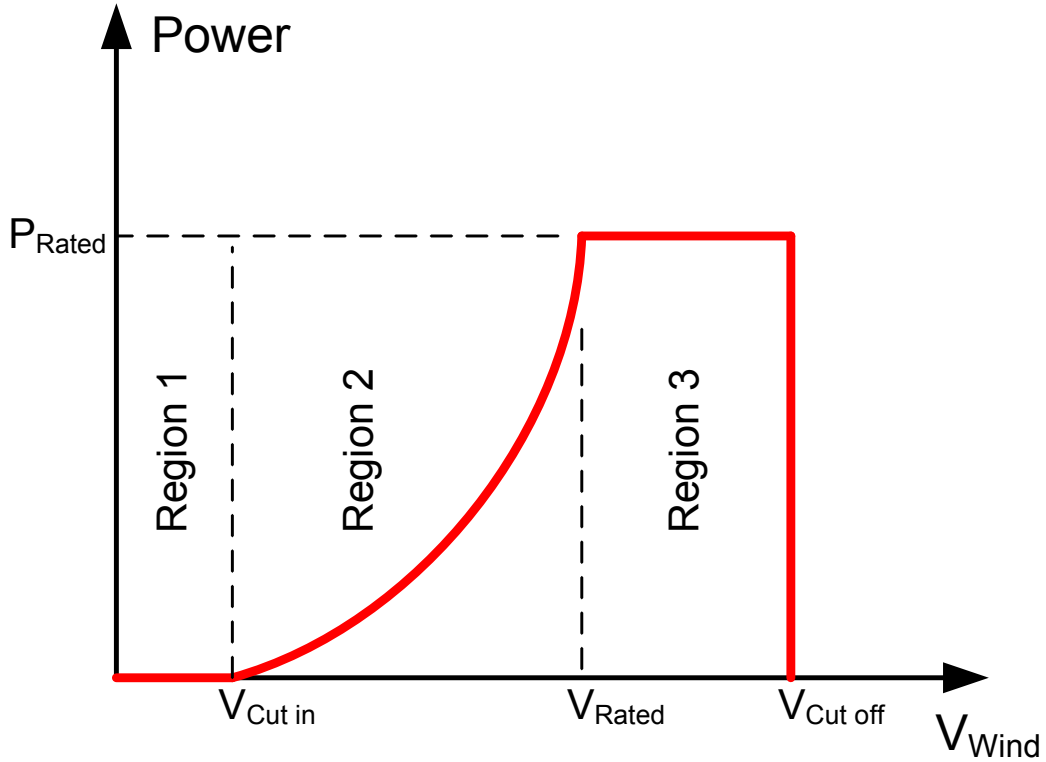
Figure 5.1: Wind Turbines Operation Regions

5.2.1 Rotor Power Coefficient – C_p

The power coefficient is a measurement of how the wind turbine converts the wind energy into electrical energy efficiently. According to the *Rankine-Froude Actuator Disc Theory* and *Betz Limit* [17], using an approach simpler than the *BEM theory*, presented in section 4.1, it possible to define the following relationship:

$$P_{wind} = \frac{1}{2}\rho_{air}\, AV_0^3 \tag{5.1}$$

where ρ_{air} is the air density, A is the rotor sweep area and V_0 is the wind speed.

The aerodynamic power, P_A, can be found as:

$$P_A = P_{wind}\, C_p(\lambda, \beta, \alpha) \tag{5.2}$$

where C_p is a function of the blade pitch, β, of the platform pitch, α, and of the Tip–Speed Ratio (TSR), λ, which is defined as:

$$\lambda = \frac{\Omega R}{V_0} \tag{5.3}$$

where Ω is the rotor angular speed and R is the rotor radius.

The typical power coefficient map for this wind turbine model has been obtained running FAST with *AeroDyn* simulations at a given rotor speed ($\Omega_0 = 12.1 \, \text{rpm}$), collective blade-pitch angle ($0 \, \text{deg}$ to $30 \, \text{deg}$), platform pitch ($0 \, \text{deg}$ to $5 \, \text{deg}$), and with a wind specific speed ramp. From these simulations it has been found that the peak power coefficient of 0.4906 occurred at a tip-speed ratio of 8.1692 and with a rotor collective pitch angle of 0.0 deg.

(a) *Power Coefficient Maps* (b) *Real Power Maps*
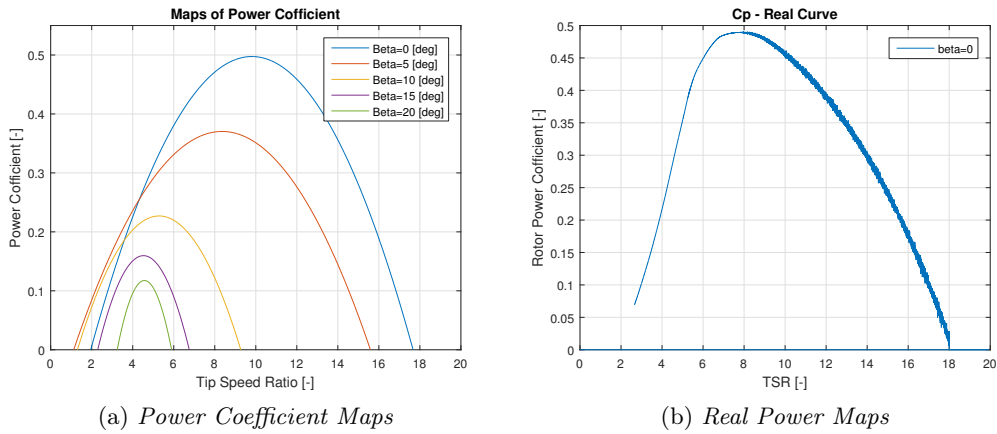
Figure 5.2: Power Coefficient

Hence:

- $C_{p_{max}} = 0.4906$

- $\lambda_{opt} = 8.1692$

5.2.2 Optimal Constant in Region 2

In region 2, it is necessary to maximize the power production. On these premises, it has been found the optimal value of K_{opt} to get the maximum power keeping the optimal tip-speed ratio.
Using the previous values of C_p and λ, the optimal value of K (HSS side) can be defined as in [10], namely:

$$K_{opt} = \frac{1}{2}\pi\rho R^5 \frac{C_{p_{max}}}{(\lambda_{opt}N_G)^3} = 0.0256 \, \text{Nm/rpm}^2 \tag{5.4}$$

where $N_G = 97$ is the HSS/LSS gearbox ratio.
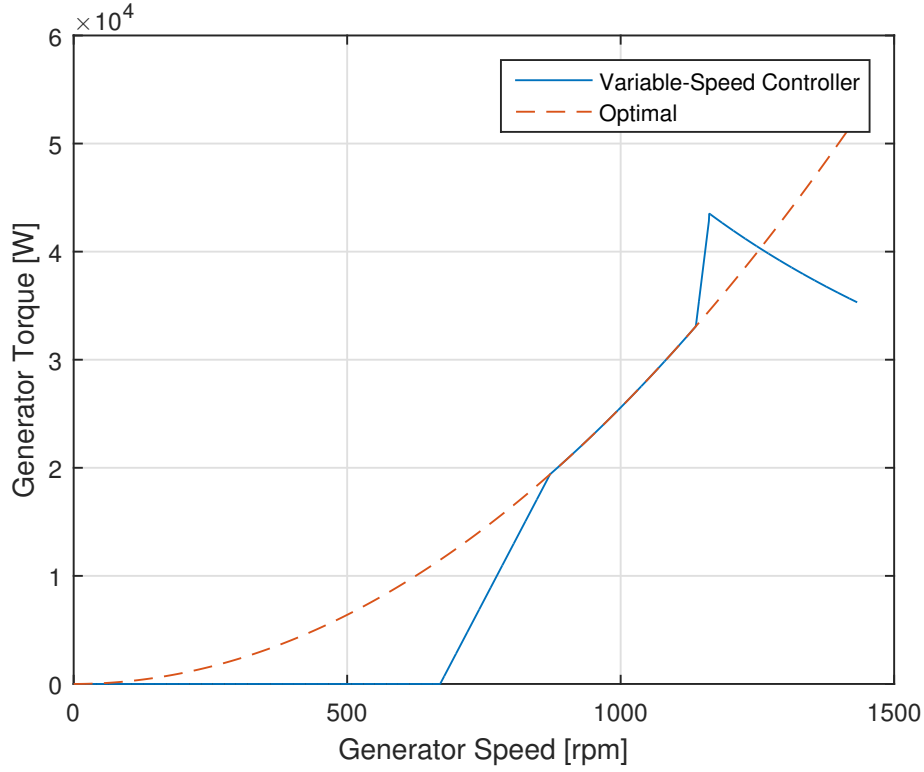
Figure 5.3: Variable-Speed Controller

5.3 Gain Scheduling PI

The first control type adopted is the full-span rotor collective blade pitch angle command. It uses a gain-scheduled proportional-integral (GSPI) control on the speed error between rotor speed and rated rotor speed, as indicated in [18]. Considering a simple single degree of freedom model and a rigid drivetrain, the motion equation can be described as follows:

$$T_A - N_G T_G = (I_R + N_G^2 I_G)\frac{d}{dt}(\Omega_0 + \Delta\Omega) = I_D\Delta\dot{\Omega} \tag{5.5}$$

where t is the simulation time, T_A is the LSS (Low-Speed Shaft) aerodynamic torque, T_G is the HSS (High-Speed Shaft) generator torque, N_G is the gearbox ratio defined above, I_D is the drivetrain inertia cast to LSS part, I_R is the rotor inertia, I_G is the generator inertia relative to HSS part, Ω_0 is the rated LSS rotational speed and $\Delta\dot{\Omega}$ is the perturbed LSS rotational acceleration.

Using a Proportional-Integral-Derivative control (PID), it is possible to define the perturbed blade pitch angle, $\Delta\beta$:

$$\Delta\beta = K_P N_G \Delta\Omega + K_I \int_0^t N_G \Delta\Omega dt + K_D N_G \Delta\dot{\Omega} \tag{5.6}$$

where K_P, K_I and K_D are the controller proportional, integral, and derivative gains, respectively.

In Region 3, as shown in figure (5.3), the generator torque controller maintains the generator power steady and the generator torque is inversely proportional to the generator speed:

$$T_G(N_G\Omega) = \frac{P_0}{N_G\Omega} \tag{5.7}$$

where Ω is the LSS rotational speed and P_0 is the rated mechanical power.

Similarly, assuming $\frac{\partial T_A}{\partial \Omega} \simeq 0$, the aerodynamic torque becomes:

$$T_A(\beta) = \frac{P(\beta, \Omega_0)}{\Omega_0} \tag{5.8}$$

where β is the collective blade pitch angle and P is the mechanical power.

Expanding the eqs. (5.7) and (5.8) using the first-order Taylor series, it emerges that:

$$T_G \simeq \frac{P_0}{N_G\Omega_0} - \frac{P_0}{N_G\Omega_0^2}\Delta\Omega \tag{5.9}$$

and

$$T_A \simeq \frac{P_0}{\Omega_0} + \frac{1}{\Omega_0}\left(\frac{\partial P}{\partial \beta}\right)\Delta\beta \tag{5.10}$$

where $\Delta\beta$ is a small perturbation of the blade pitch angle about their operating point. Hence, setting $\dot{\eta} = \Delta\Omega$ and combining the eqs. (5.9) and (5.10) with the eqs. (5.6) and (5.5), the rotor speed error equation becomes:

$$\underbrace{\left[I_D + \frac{1}{\Omega_0}\left(-\frac{\partial P}{\partial \beta}\right)N_G K_D\right]}_{M_\eta}\ddot{\eta} + \underbrace{\left[\frac{1}{\Omega_0}\left(-\frac{\partial P}{\partial \beta}\right)N_G K_P - \frac{P_0}{\Omega_0^2}\right]}_{C_\eta}\dot{\eta} + \underbrace{\left[\frac{1}{\Omega_0}\left(-\frac{\partial P}{\partial \beta}\right)N_G K_I\right]}_{K_\eta}\eta = 0$$

$$\tag{5.11}$$

The PID controlled rotor speed error responds as a second-order system with a damping ratio, ζ_η and a natural frequency, $\omega_{\eta n}$, equal to:

$$\omega_{\eta n} = \sqrt{\frac{K_\eta}{M_\eta}} \tag{5.12}$$

and

$$\zeta_\eta = \frac{C_\eta}{2M_\eta\omega_{\eta n}} = \frac{C_\eta}{2\sqrt{K_\eta M_\eta}} \tag{5.13}$$

In region 3, $\frac{\partial P}{\partial \beta}$ is negative. Thus, choosing a positive control gains, the derivative term increases the effective inertia, the proportional term adds damping and the integral term increases the stiffness term. Furthermore, the generator torque controller introduces a negative damping by the term $-P_0/\Omega_0^2$ in equation (5.11). Such a negative damping must be compensated by the proportional term K_P included in the blade pitch controller.

In the design of the blade pitch control, the controller-response natural frequency and damping ratio have been chosen equals to 0.2 rad/sec and 0.7,

respectively. As in [30], [18] and [23], the derivative term and the negative dumping, introduced from the generator torque, have been neglected. Adopting $\omega_{\eta n} = 0.2$ rad/sec and $\zeta_\eta = 0.7$, as stated in [22], ensures a controller-response natural frequency lower than the smallest critical structure natural frequency. Moreover, as demonstrated in [33], such assumptions ensure that the support platform motions remain positively damped.

These specifications lead to a direct expression for an appropriate choice of the PI gains once that the sensitivity of aerodynamic power to collective blade pitch, $\frac{\partial P}{\partial \beta}$, is known:

$$K_P = \frac{2 I_D \Omega_0 \beta_\eta \omega_{\eta n}}{N_G \left(-\frac{\partial P}{\partial \beta} \right)} \tag{5.14}$$

and

$$K_I = \frac{I_D \Omega_0 \omega_{\eta n}^2}{N_G \left(-\frac{\partial P}{\partial \beta} \right)} \tag{5.15}$$

The blade pitch sensitivity, $\frac{\partial P}{\partial \beta}$, is an aerodynamic property of the rotor that depends on the rotor speed, the wind speed and the blade pitch angle. It has been calculated by performing a linearization analysis in FAST with: i) AeroDyn at a number of given steady and uniform wind speed and ii) considering only one DOF enabled (GeAz_DOF). Hence, since the rotor speed has been fixed at the rated value ($\Omega_0 = 12.1$rpm), the corresponding pitch angle has been found thought a trim analysis. It returns the pitch angle necessary to produce a rated mechanical power ($P_0 = 5.296619$ MW) [18].

Wind Speed	Rotor Speed	Pitch Angle	$\partial P / \partial \beta$
(m/s)	(rpm)	(deg)	(watt/rad)
11.4	12.1	0.00	-28.25E+06
12.0	12.1	4.15	-43.98E+06
13.0	12.1	6.67	-52.00E+06
14.0	12.1	8.82	-58.45E+06
15.0	12.1	10.54	-63.92E+06
16.0	12.1	12.15	-70.30E+06
17.0	12.1	13.64	-76.30E+06
18.0	12.1	14.90	-84.02E+06
19.0	12.1	16.33	-90.71E+06
20.0	12.1	17.59	-94.65E+06
21.0	12.1	18.79	-100.00E+06
22.0	12.1	19.94	-106.01E+06
23.0	12.1	21.08	-114.60E+06
24.0	12.1	22.17	-120.22E+06
25.0	12.1	23.20	-125.40E+06

Table 5.1: Sensitivity of Aerodynamic Power to Blade Pitch in Region 3
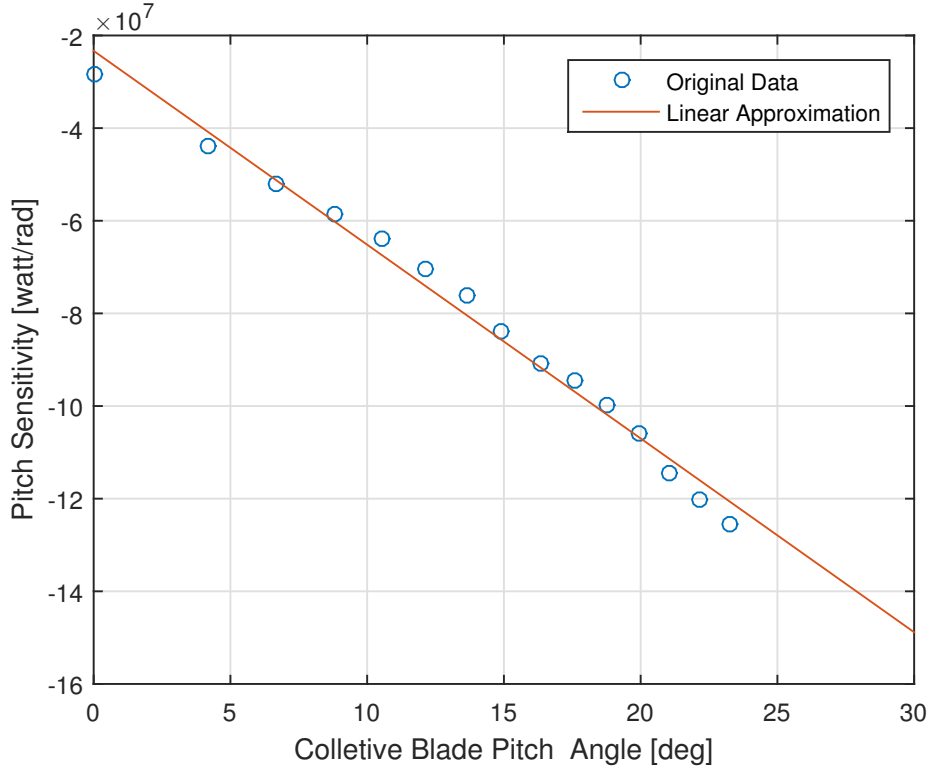
Figure 5.4: Linear Approximation of pitch sensitivity in Region 3

In table (5.1) it is possible to see that $\left(\frac{\partial P}{\partial \beta}\right)$ is a highly variable term, hence constant PI gains are not adequate for effective speed control. Furthermore, it can be also observed that $\left(\frac{\partial P}{\partial \beta}\right)$ is characterized by a downward trend respect the blade pitch angle.

Plotting the results (fig. 5.4), it is easy to see that the pitch sensitivity varies linearly with blade pitch angle. By applying a linear regression it is possible to affirm that:

$$\frac{\partial P}{\partial \beta} = \left[\frac{\frac{\partial P}{\partial \beta}(\beta = 0)}{\beta_K}\right]\beta + \left[\frac{\partial P}{\partial \beta}(\beta = 0)\right] \tag{5.16}$$

where $\frac{\partial P}{\partial \beta}(\beta = 0)$ is the pitch sensitivity at rated and β_K is the blade pitch angle at which the pitch sensitivity has doubled its value respect to the rated operating point. Hence, before these considerations:

$$\frac{\partial P}{\partial \beta}(\beta = \beta_K) = 2\frac{\partial P}{\partial \beta}(\beta = 0) \tag{5.17}$$

where $\beta_K = 5.577$ deg with $\frac{\partial P}{\partial \beta}(\beta = 0) = -28.25E + 06$ watt/rad.

The linear relation between pitch sensitivity and blade pitch angle presents a simple technique for implementing a gain scheduling. As a consequence equations (5.14) and (5.15) become:

$$K_P(\beta) = \frac{2I_D\Omega_0\zeta_\varphi\omega_{\varphi n}}{N_G\left[-\frac{\partial P}{\partial \beta}(\beta = 0)\right]}GK(\beta) \tag{5.18}$$

44

and

$$K_I(\beta) = \frac{I_D \Omega_0 \omega_{\varphi n}^2}{N_G \left[-\frac{\partial P}{\partial \beta}(\beta = 0) \right]} GK(\beta) \tag{5.19}$$

where $GK(\beta)$ is the dimensionless gain corrector factor, which depends on the blade pitch angle according to the following relationship:

$$GK(\beta) = \frac{1}{1 + \frac{\beta}{\beta_K}} \tag{5.20}$$

Figure (5.5) shows the K_P, K_I and GK trends as functions of the blade pitch angle, β (hundred factor is only to a graphic matter).
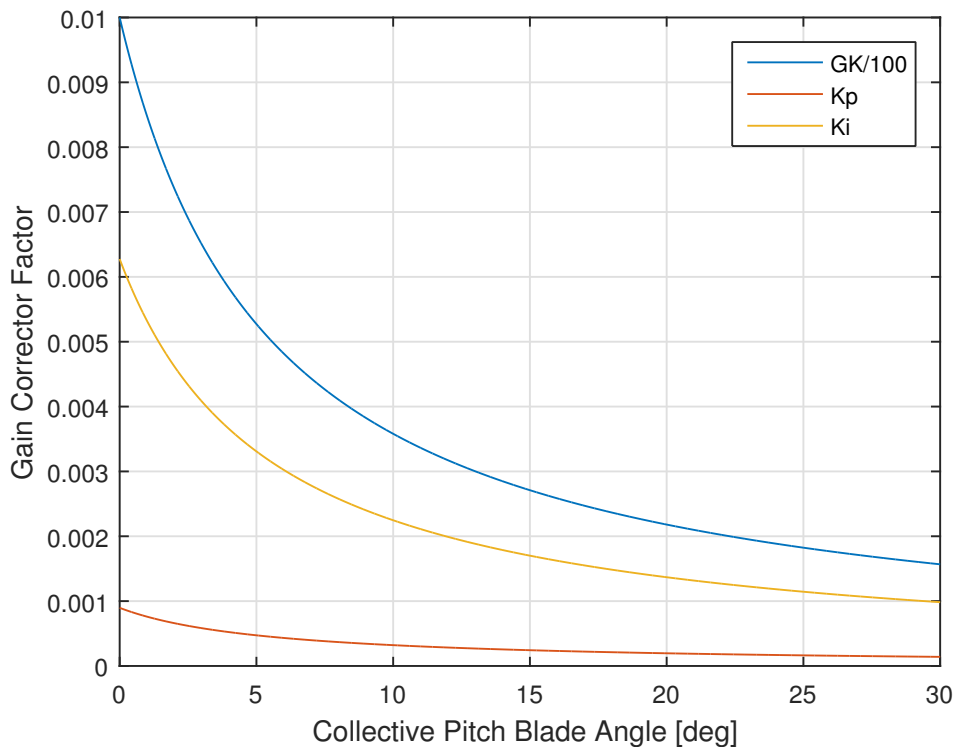
Figure 5.5: Blade Pitch Control Gain Scheduling Law

where:

- $K_P(\beta = 0) = 0.006$

- $K_I(\beta = 0) = 0.0009$

During the implementation of the *GSPI*, the blade pitch angle from the previous controller time-step has been used to calculate the gain-correction factor at the next time step. After a first implementation with a power constant generator control, another control law with a constant generator torque, as in [22], has been implemented. This change does not introduce negative damping in the rotor speed response, namely the term $\left(\frac{P_0}{\Omega_0} \right)$ is equal to *zero*,

but reduces the rotor speed excursion that has been exaggerated by a very little proportional gain. Furthermore, a blade pitch angle limit from 0 to 90 deg and a blade pitch rate limit range to $[-8, +8]$ deg/sec, which is a conventional limits of a 5–MW machines, have been set.

5.4 LQR Control with Collective Blade Pitch

This section describes another control type that have been implemented to realise the collective blade pitch control (CBP). In this case, the control is based on a Space State Controller using a Linear Quadratic Regulator (LQR) defined in [25]. This control type is a MIMO controller that allows achieving more goals, which can be split in primary and secondary objectives:

- Primary goals:
  - Reduction of rotor speed oscillation
  - Reduction of platform pitch oscillation

- Secondary goals:
  - Reduction of tower-top fore-aft oscillation
  - Reduction of tower-top side-to-side oscillation

LQR is a linear controller strategy, which requires a linear representation of the floating wind turbine. As explained in Appendix A, FAST has the capability to extract a linearized representation of the complete nonlinear wind turbine model. The model complexity depends on the control objectives. As explained in ([15], [29]) a 8–DOFs linear state space is adequate to account for the platform pitch dynamics.
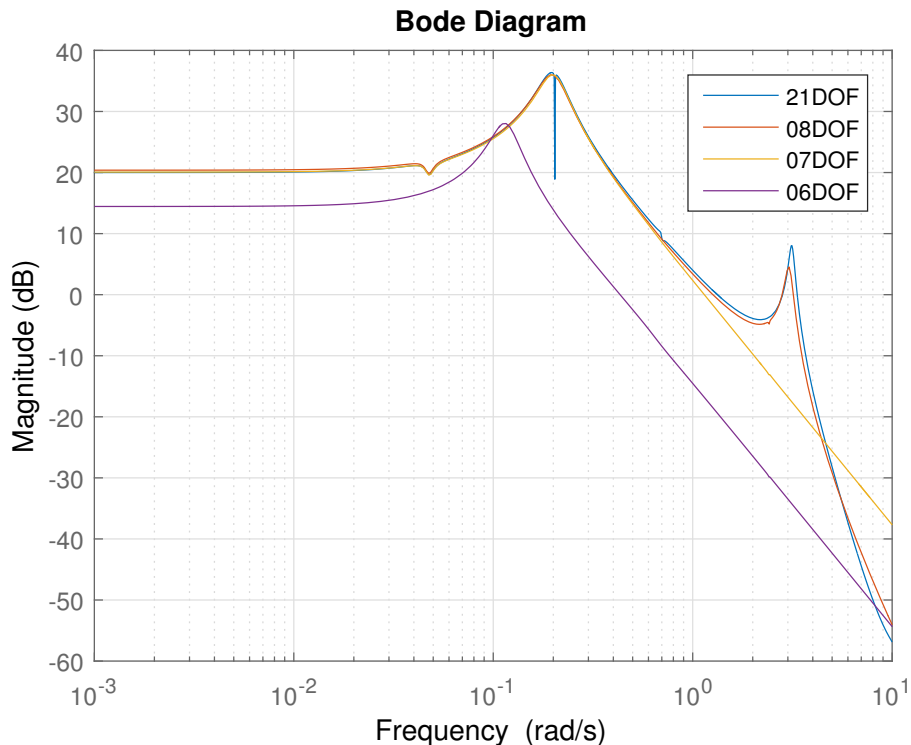
Figure 5.6: Platform pitch frequency response to collective blade pitch

Considering a model with 6–DOFs, namely without considering the platform surge DOF, the first platform pitch peak resonant frequency (it should

Enabled DOFs	Description
6	Platform roll, pitch and yaw, first tower side-to-side, rotor and drivetrain
7	6 DOFs + platform surge
8	7 DOFs + first tower fore-aft
21	All DOFs except nacelle yaw

Table 5.2: DOFs List for figure 5.6

not be confused with the natural frequency) changes by 68% if compared with a 21–DOFs enabled. The effects of adding certain DOFs to the linearized state-space model (for control design) are shown in figure (5.6). Indeed, including the surge DOF, the correct peak is attained and the low-frequency gain results closer to the actual system (21–DOFs). The addition of the fore-aft tower bending DOF, accounts for the second resonant peak that is in close proximity to the first. Therefore, using a State Feedback Control (SFC) designed with a 8–DOFs model, a good approximation can be achieved. The linear wind turbine response (21–DOFs vs 8–DOFs) reported in figure (5.7) confirms these assumptions.
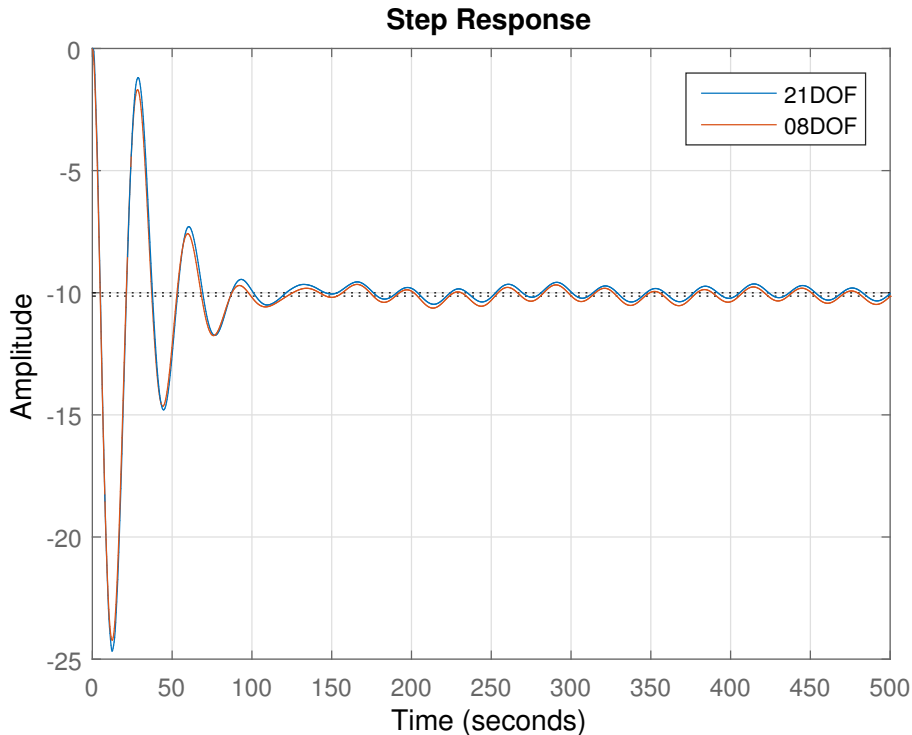
Figure 5.7: Platform pitch response to collective blade pitch step

However, as in [15], the platform surge position has been removed from the linear space state before the controller design. Since regulating the platform surge position is not considered critical to normal operation, a not necessary

blade pitch actuator increase has been avoided by removing it from the control objective.

LQR control design is applied to model design above, with system inputs: $\underline{u} = \begin{bmatrix} T_G & \beta \end{bmatrix}$. Besides this, the design of the LQR Control is straightforward: weighting the states and inputs with respect to performance objectives, by minimizing the cost function:

$$J = \int_0^\infty \left(\underline{x}^T Q \underline{x} + \underline{u}^T R \underline{u} \right) dt \tag{5.21}$$

where Q is positive semi-definite and R is positive definite. Requiring full state information, the controller calculates a system input:

$$\underline{u} = -K\underline{x} \tag{5.22}$$

where the states are multiplied by the feedback gain matrix K that has been calculated solving the Differential Riccati Equation (DRE).

The implemented controller has the following weight matrices:

$$Q = diag\Big(\frac{10}{(0.2x_{op,i})^2}, \frac{10}{(0.2x_{op,i})^2}, 0, \frac{1}{(0.2x_{op,i})^2}, \frac{1}{(0.2x_{op,i})^2}, \frac{1}{50^2},$$
$$0, 0, 0, 5, 0, 1, 1, \frac{10}{(0.1x_{op,i})^2}, \frac{1}{0.05^2} \Big) \quad \text{with i=1,\dots,15} \tag{5.23}$$

and

$$R = diag\Big(\frac{100}{(0.2u_{op,i})^2}, \frac{100}{(0.2u_{op,i})^2} \Big) \quad \text{with i=1,2} \tag{5.24}$$

5.5 DAC with Collective Blade Pitch

Disturbance Accommodating Control (DAC) is a type of feed-forward control used to minimise or cancel the effects of a persistent disturbance. In this case it will be used to reduce the effects introduced by the wind speed perturbation. As implemented in [16] and [29], DAC has been obtained by augmenting the linearized state matrices to recreate the disturbance through an assumed waveform. The linear system, given by eq. (A.12), will be extended with the disturbance input vector, u_d, and with its equivalent disturbance gain matrix, B_d. The disturbance wave model waveform is modelled with the following system:

$$\begin{aligned} \dot{\underline{z}} &= F\underline{z} \\ \underline{u}_d &= \Theta\underline{z} \end{aligned} \tag{5.25}$$

where F and Θ are assumed to be known but with unknown initial condition. As in [14], for simplicity, a step change waveform model is used for wind speed perturbation about the operating point. The parameters are the following:

$$\text{step input} = \begin{cases} \Gamma = 1 \\ \Theta = 0 \end{cases} \tag{5.26}$$

Connecting the eqs. (5.25) and (A.12) the disturbance accommodating control law is formed by:

$$\underline{u}^* = K\,\underline{x} + K_d\,\underline{z} \tag{5.27}$$

where $\underline{u}^*$ is the combined effect of the controller gain matrix, K, and the disturbance controller gain matrix, K_d. The equation above has two terms: the first is the state regulator, calculated by LQR, and the second is the DAC component that minimizes the effects of persistent disturbances. Substituting the $\underline{u}^*$ expression into the system state equations, the following relationship is given:

$$\underline{\dot{x}} = (A + BK)\underline{x} + (B_d\Theta + BK_d)\underline{z} \tag{5.28}$$

in which, imposing:

$$(BK_d + B_d\Theta) = 0 \tag{5.29}$$

thus:

$$K_d = -B^+ B_d\Theta \tag{5.30}$$

where B^+ is the Moore-Penrose pseudo-inverse matrix of B.

This controller has been implemented using the same weight matrices, Q and R, adopted in the LQR–CBP. Furthermore it has been assumed that the height hub wind speed should be measured by an anemometer placed on the wind turbine nacelle. Introducing this hypothesis, it is not necessary to use a wind speed estimator.

5.5.1   Collective Blade Pitch Drift

The collective blade pitch drift is an existing issue analysed in [29]. Implementing a DAC to reject wind speed perturbation. Assuming a linear wind turbine system, the collective blade pitch commanded by a feed-forward action of the DAC is a linear function of the wind speed described in equation (5.27). This equation represents the collective blade pitch perturbed command about a linearized operating point, the final value is obtained adding up the operative point, $u_{op} = f(v_{\text{wind}})$.

The collective blade pitch angle required to keep the floating wind turbine in steady state, is not a wind speed linear function, as shown in figure (5.8). With steady state conditions, DAC forces the collective blade pitch away from the optimum angle as the turbine operates away from the linearization point.

Considering the wind speed time series, shown in figure (2.6), the wind speed range is about 16 m/sec and oscillates from 8 to 25 meters per second. The analysis of the figure (5.8), shows that especially for wind speed lower than 17 m/sec the DAC linearization curve does not follow the non linear collective blade pitch angle.
A solution to overcome this issue is to use a scheduled collective blade pitching component that follows the non linear optimum trajectory for rotor speed regulation.
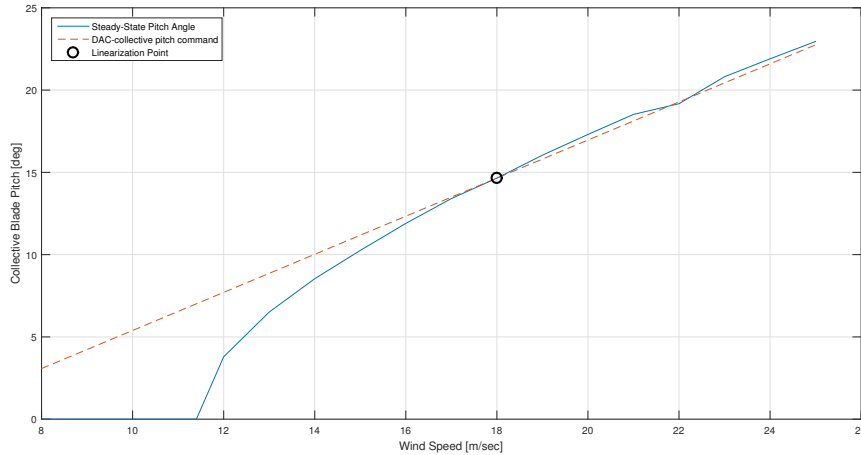
Figure 5.8: Collective Blade Pitch Drift

5.6 LQR Control with Individual Pitch Blade

Both GSPI and LQR–CBP controls strategies use the collective blade pitch angle to regulate the system. Another mechanism, as the individual pitch blade (IBP), allows to restore the platform pitch creating asymmetric aerodynamic loads in addition to the symmetric load, thus enhancing the platform pitch restoring moment.

The mechanism can be explained looking at the periodic gain matrix reported in figure (5.10). The gain for blade 1 is negative for azimuth angles approximately between 90 and 270 degrees, when the blade is in the lower half of the rotor. Therefore, supposing a negative platform pitch velocity ($\partial \dot{x} < 0$), as in figure (5.9), blades at the top with a positive control gain will be used to decrease blade pitch, hence increasing the thrust. Blades at the bottom with negative controller gain will be used to increase blade pitch, thus reducing thrust. The periodic gain that corresponds to the platform pitch state is not shown. Moreover, it has the same shape of the fig. (5.10) when it is emphasized in the weight matrix, Q.
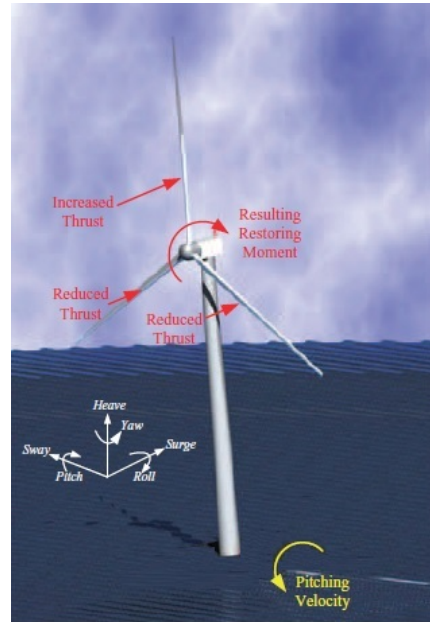
Figure 5.9: Platform Pitch restoring mechanism using IBP

The only difference respect to the CBP model is to consider each pitch blade angle controllable separately. This increases the number of available actuators from 2 to 4 (for a three blades wind turbine and including the generator torque). However, there are some issues that arise implementing the IBP

51
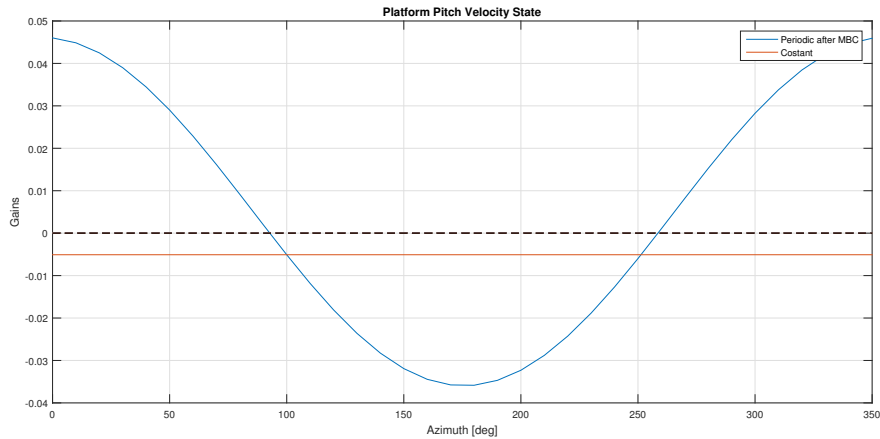
Figure 5.10: Blade 1 periodic gain and constant gain

controller, which are:

- Increased blade pitch actuation which may result in blade pitch saturation.

- Setting too high weight in Q, R matrices may produce an increase of the blade load.

- The possibility of exciting or destabilising other turbine modes due to coupling with no modelled DOFs.

The issues above involve a more careful choice of Q and R matrices. With this setting is not possible to use a control system based on a LTI model. Since the control law depends on the blade position on the rotor plane, it needs a periodic model in function of the rotor azimuth angle. To avoid this increase of complexity, the MBC transformation allows to implement a control system based on a LTI model even though the model periodicity.

5.6.1 Multi-Blade Coordinate Transformation - MBC

The wind turbine dynamics like rotor blades are generally expressed in rotating frame attached to the individual blades. The tower and nacelle subsystem are affected by the combined effect of all rotor blades, not the individual blades. This is because the rotor responds as a whole to excitations such as aerodynamics gusts, control inputs and tower-nacelle motion, all of which occurring a non-rotating frame. MBC transformation, defined in [4], expresses the dynamics of individual blades in a fixed (non-rotating) frame. MBC offer several benefits:

- Providing the exact dynamic interaction between the non-rotating tower-nacelle and the spinning rotor.

- Offering insights concerning rotor dynamics and the way the rotor interacts with fixed-system entities, such as wind, controls, tower and nacelle subsystem.

- Removing all periodic terms except those which are integral multiples of ΩB, where Ω is the rotor angular speed and B is the number of the rotor blades.

MBC Concept and Associated Transformation – Considering a rotor with B blades that are spaced equally around the rotor disk, the azimuth location of the bth blade is given by:

$$\Psi_b = \Psi + (b-1)\frac{2\pi}{B} \qquad (5.31)$$

where Ψ is the azimuth of the first (reference) blade and it is assumed equal to *zero*, implying that the first blade is vertically up. Since the number of blades is $B = 3$ and the MBC is a linear transformation, which relates the rotating degrees of freedom to new degrees of freedom, they are defined as:

Figure 5.11: MBC Coordinate Transformation

$$q_0 = \frac{1}{B}\sum_{b=1}^{B} q_b$$

$$q_c = \frac{2}{3}\sum_{b=1}^{B} q_b \cos\Psi_b \qquad (5.32)$$

$$q_s = \frac{2}{3}\sum_{b=1}^{B} q_b \sin\Psi_b$$

where q_0 is the collective mode, q_c is the cosine-cyclic mode and q_s is the sine-cyclic mode. The equations in (5.32) determine the rotor coordinate, given the blades coordinates. The inverse transformation yielding the blade coordinate given the rotor coordinate is:

$$q_b = q_0 + q_c \cos\Psi_b + q_s \sin\Psi_b \qquad \text{with } b = 1, 2, 3 \qquad (5.33)$$

where, in this equation and in the equations above, q_b is a particular rotating degree of freedom (more detailed informations can be found in [5]).

In the linearized representation of the 8–DOFs model, the $\underline{u}$ vector contains control inputs that are in the rotating frames references whereas the disturbance vector, $\underline{u}_d$, has been assumed to have no input in the rotating frame of reference. Applying the MBC transformation, the new transformed matrices $A_{\text{NR}}, B_{\text{NR}}, B_{d_{\text{NR}}}, C_{\text{NR}}$ and D_{NR} are obtained passing through the transformation matrices $T_s(\Psi)$, $T_c(\Psi)$ and $T_o(\Psi)$, where:

$$\underline{x} = T_s(\Psi)\underline{x}_{\text{NR}} \qquad (5.34)$$

$$\underline{u} = T_c(\Psi)\underline{u}_{\text{NR}} \qquad (5.35)$$

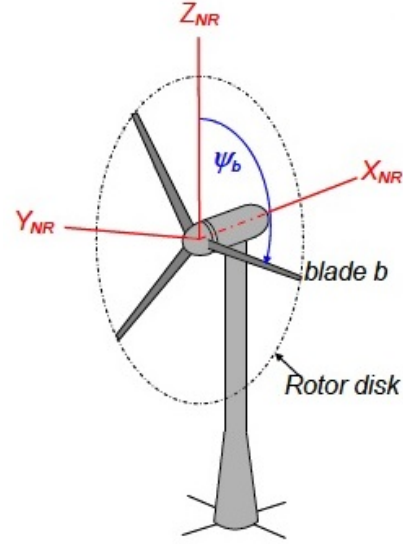$$\underline{y} = T_o(\Psi)\underline{y}_{\text{NR}} \qquad (5.36)$$

and considering:

$$\underline{u} = \begin{bmatrix} T_G & \beta_1 & \beta_2 & \beta_3 \end{bmatrix}^T \tag{5.37}$$

then,

$$T_c(\Psi) = \begin{bmatrix} 1 & 0 & 0 & 0 \\ 0 & 1 & \cos(\Psi) & \sin(\Psi) \\ 0 & 1 & \cos(\Psi + \frac{2\pi}{3}) & \sin(\Psi + \frac{2\pi}{3}) \\ 0 & 1 & \cos(\Psi + \frac{4\pi}{3}) & \sin(\Psi + \frac{4\pi}{3}) \end{bmatrix} \tag{5.38}$$

The new input vector achieved after the transformation assumes a different physic interpretation:

$$\underline{u}_{\mathrm{NR}} = \begin{bmatrix} T_G & \beta_0 & \beta_c & \beta_s \end{bmatrix}^T \tag{5.39}$$

where T_G is the same that in rotating frame, whereas β_0, β_c and β_s are the collective, cosine and sine contributions, respectively.

In this particular case, there are not states and outputs in rotating frame references, thus:

$$T_s(\Psi) = I_{n,n} \tag{5.40}$$

and

$$T_o(\Psi) = I_{p,p} \tag{5.41}$$

where I is the identical matrix, n is the number of the states and p in the number of the outputs.

5.6.2 LQR after MBC Transformation

After applying MBC Transformation on a periodic system, the LQR law in the non-rotating frame becomes:

$$\underline{u}_{\mathrm{NR}} = -K_{\mathrm{NR}} \, \underline{x}_{\mathrm{NR}} \tag{5.42}$$

Equations (5.34), (5.35) and (5.42) have been used to transform back the blade pitch commands in the mixed frame, getting the following relationship:

$$
\begin{aligned}
\underline{u} &= T_c(\Psi) \, \underline{u}_{\mathrm{NR}} \\
&= -T_c(\Psi) \, K_{\mathrm{NR}} \, \underline{x}_{\mathrm{NR}} \\
&= -T_c(\Psi) \, K_{\mathrm{NR}} \, T_s^{-1}(\Psi) \, \underline{x} \\
&= -T_c(\Psi) \, K_{\mathrm{NR}} \, I_{n,n}^{-1} \, \underline{x} \\
&= K_{\mathrm{MBC}}(\Psi) \, \underline{x}
\end{aligned}
\tag{5.43}
$$

thus,

$$K_{\mathrm{MBC}}(\Psi) = -T_c(\Psi) \, K_{\mathrm{NR}} \, I_{n,n} \tag{5.44}$$

5.7 DAC with Individual Blade Pitch

This section presents the Disturbance Accommodation Control (DAC) based on Individual Blade Pitch. The basic rules are the same as explained in section 5.5.

Using an individual blade pitch, where the control is azimuth angle dependent, it is possible to include the wind share effect. Wind share describes the horizontal increase of the wind speed with the height. It is expected that, by including this effect in the linearized models, especially for periodic controller, the performance of the wind turbine will improve.

5.7.1 Including Wind Share Effect

To develop a wind-share linearized model, the same approach as in [34] has been used. The wind-speed variation with height is expressed as:

$$V(z) = V_{hub}\left(1 + \frac{z}{H}\right)^m \tag{5.45}$$

where V_{hub} is the wind speed at hub-height, H, z is the height above the hub and the coefficient m is the power wind-shear coefficient, defined in section 2.4.1.

Equation (5.45) can be expressed as a binomial series in $\left(\frac{z}{H}\right)$:

$$\left(1 + \frac{z}{H}\right)^m = 1 + m\left(\frac{z}{H}\right) + \frac{m(m-1)}{2}\left(\frac{z}{H}\right)^2 + \frac{m(m-1)(m-2)}{6}\left(\frac{z}{H}\right)^3 + \dots \tag{5.46}$$

Using the polar coordinates (R and Ψ), z becomes:

$$z = R\cos(\Psi) \tag{5.47}$$

where, R is the rotor radius and Ψ is the rotor azimuth angle.

Substituting equation (5.47) in equation (5.46), and considering until the third-order terms, the following expression results, involving in: V_{hub}, H, R, m and Ψ:

$$V(R,\Psi) \cong \frac{V_{hub}}{6h^3}\left[6h^3 + 6h^2 mR\cos(\Psi) + 3hm(m-1)R^2\cos^2(\Psi) + m(m-1)(m-2)R^3\cos^3(\Psi)\right] \tag{5.48}$$

For the OC3–Hwind the equation (5.48) becomes:

$$V(R,\Psi) \cong V_{hub}\left[0.97 + 0.115\cos(\Psi) - 0.004\cos(3\Psi)\right] \tag{5.49}$$

where the dominant periodic term is $0.115\cos(\Psi)$, thus the other term will be neglected.

The first term in equation (5.49) is the wind component, which is no dependent on azimuth position and it will be modelled with the DAC step waveform. The second term represents the azimuth-dependent component. This additional term, not present in the DAC–CBP, must be represented with a new DAC waveform.

To represent this new term, the matrices of the general disturbance wave model, in eq (5.25), become:

$$\Theta = \begin{bmatrix} 1 & 0 & 0 \\ 0 & 1 & 0 \end{bmatrix}, \qquad F = \begin{bmatrix} 0 & 0 & 0 \\ 0 & 0 & 1 \\ 0 & -\Omega^2 & 0 \end{bmatrix} \tag{5.50}$$

these matrices were achieved using the following variables:

$$\begin{aligned} u_{d,1} &= z_{d,1} \\ u_{d,2} &= z_{d,2} = A_d \cos(\Psi) = A_d \cos(\Omega t) \\ z_{d,3} &= \dot{z}_{d,2} \end{aligned} \tag{5.51}$$

where $A_d = 0.115\, V_{hub}$ and $\Psi = \Omega t$.

5.7.2 DAC after MBC Transformation

In this work the disturbance states, $\underline{z}$, are modelled in the non-rotating frame. Such assumption avoids their transformation from the rotating frame. After MBC transformation on a periodic system, DAC design becomes time-invariant. The DAC law in the non-rotating frame is given by equation (5.52) and the time-invariant DAC gain is found by solving the equation (5.53).

$$\underline{u}_{\text{NR}} = -K_{\text{NR}}\underline{x}_{\text{NR}} + K_{d_{\text{NR}}}\underline{z} \tag{5.52}$$

$$K_{d_{\text{NR}}} = -B_{\text{NR}}^{+} B_{d_{\text{NR}}}\Theta \tag{5.53}$$

The DAC law is now in the non-rotating frame and therefore, blade pitch command have to be transformed back to mixed frame. Using equations (5.35), (5.52) and (5.53) the following relationship has been achieved:

$$\begin{aligned} \underline{u} &= -T_c(\Psi)\, K_{\text{NR}}\, T_s^{-1}(\Psi)\, \underline{x} + T_c(\Psi) K_{d_{\text{NR}}}\, \underline{z} \\ &= -T_c(\Psi)\, K_{\text{NR}}\, I_{n,n}^{-1}\, \underline{x} + K_{d_{\text{MBC}}}(\Psi)\, \underline{z} \\ &= K_{\text{MBC}}(\Psi)\,\underline{x} + K_{d_{\text{MBC}}}(\Psi)\,\underline{z} \end{aligned} \tag{5.54}$$

where $K_{\text{MBC}}(\Psi)$ is the same as in equation (5.44).

In a control model considering IBP command and MBC transformation, despite what affirmed said about the collective blade pitch drift in section 5.5.1, it is easily possible to overcome the problem, as in [14], where the element in the $K_{d_{\text{NR}}}$ vector corresponding to collective blade pitch, that is β_0 in equation (5.39) has been zeroing. Removing this gain components, the DAC controller tries to compensate the wind speed perturbations using the cosine- and sine-cyclic pitch. Furthermore, to force the state-space part of the DAC to only remove the residual periodic effects, some elements in the $B_{d_{\text{NR}}}$ must be set to *zero*. These states are those corresponding to drivetrain state and to any other state on which the periodic blade pitching has a limited control authority.

This controller has been implemented using the same weight matrices, Q and R, used in LQR–IBP.

Chapter 6

Results

In this chapter the results of several simulations achieved using the NREL FAST within Matlab Simulink are presented. The control systems explained in the previous chapter have been tested on the created wind turbine structure using a non linear system with 21–DOFs enabled (Nacelle–Yaw DOF has not been taken into account since the wind direction has been considered aligned with the rotor axis). To facilitate the comparisons between all simulations, the wind turbine structure has been exposed with the same exogenous inputs, namely the wind and wave temporal series shown in figures (2.6) and (2.7), respectively. To comply with the IEC 61400–3 standard, as stated in [1], as well as to compute a load and fatigue analysis [27], the simulation time has been selected equal to 630 seconds. However, the first 30 seconds of simulation data achieved have not been recorded. The time-step integrator, DT, should be set less than or equal to one over ten times the highest full system natural frequency. To calculate the full system natural frequency the Campbell Diagram has been adopted. It allows the identification of the energy contribution that each DOF has on each mode of the overall coupled system.

Mode	Nat. Freq. [Hz]	Mode	Nat. Freq. [Hz]
Platform Surge	0.0081	1st BldFlap Collective	0.7103
Platform Sway	0.0081	1st BldEdge Sine	1.0818
Platform Heave	0.0324	1st BldEdge Cosine	1.0952
Platform Roll	0.0340	2nd BldFlap Cosine	1.9327
Platform Pitch	0.0340	2nd BldFlap Sine	2.0176
Platform Yaw	0.1210	2nd BldFlap Collective	2.0233
1st Tower Side-to-Side	0.4578	1st Drivetrain	2.9624
1st Tower Fore-Aft	0.4732	1st BldEdge Collective	3.4759
1st BldFlap Cosine	0.6784	2nd Tower Fore-Aft	3.7511
1st BldFlap Sine	0.7032	2nd Tower Side-to-Side	4.2672

Table 6.1: OC3-Hywind Natural Frequencies

In the OC3-Hywind model the highest full system natural frequency is 4.2672 Hz, that corresponds to the second side-to-side tower blending mode. Hence, a DT value equal to 0.0125 seconds is sufficiently small to consider all structure dynamics.

Ten performances indices have been used to evaluate the simulated controllers qualities. Three types of different calculations have been carried out: Mean Value, RMS (Root Mean Square) and Damage Equivalent Load (DEL). The Damage Equivalent Load calculation is explained in Appendix B.

A brief description of each performance index is given below:

- The Mean Rotor Speed is used to evaluate the reference tracking on rotor speed.

- The RMS of the Rotor Speed Error (from rated speed). The lower the value, the better the rotor speed regulation.

- The Mean Generator Power is used to evaluate the reference tracking on generator power.

- The RMS of the Generator Power Error (from rated power). The smaller the error, the better the power regulation, and thus the higher the power quality.

- The RMS of the Platform Roll is used to evaluate the platform rotation about its roll axis. This index should be kept as low as possible to reduce the tower side-to-side bending loads.

- The RMS of the Platfrom Pitch evaluates the platform rotation about its pitch axis. This parameter should be kept as low as possible to reduce the tower fore-aft bending load.

- The Maximum RMS of the Blade Pitch Rate is used to indicate the actuator usage. A high value means a high use of the blade pitch actuator.

- The Tower-Base Fore-Aft (FA) Bending fatigue DEL.

- The Tower-Base Side-to-Side (SS) Bending fatigue DEL.

- The LSS DEL indicates total rotating LSS bending moment DEL in kN-m.

6.1 Results Comparisons

Table (6.2) reports the mean values and their respective errors. These indices can be used to asses the fundamental objectives, that are 5 MW of produced power and a rotor rotational speed of 12.1 rpm.

| Indices | | Control Types | | | | |
Name	Unit	GSPI	LQR–CBP	DAC–CBP	LQR–IBP	DAC–IBP
Mean Rotor Speed	rpm	12.150	12.123	12.105	12.096	12.1015
Rotor Speed Err.	rpm	0.050	0.023	0.005	0.004	0.002
Mean Gen. Power	MW	5.209	5.010	5.001	5.00	5,00
Gen. Power Err.	MW	0.209	0.010	0.001	0.00	0.00

Table 6.2: Mean values and their respective errors

The first comparison has been done between GSPI and LQR–CBP controllers. As shown in figure (6.1) the three main outputs used to evaluate the different control qualities have been compared in terms of time series. The rotor speed, the generator power and the platform pitch present a better trend in LQR–CBP with respect to the GSPI control, as expected. Indeed, with a LQ Regulator it is possible to set more control objectives, on the contrary the Baseline GSPI assumes only the rotor speed regulation. Furthermore, the controllers have been developed using different wind turbine control models, where obviously the 8–DOFs have the best capability to reproduce the real wind turbine trend.
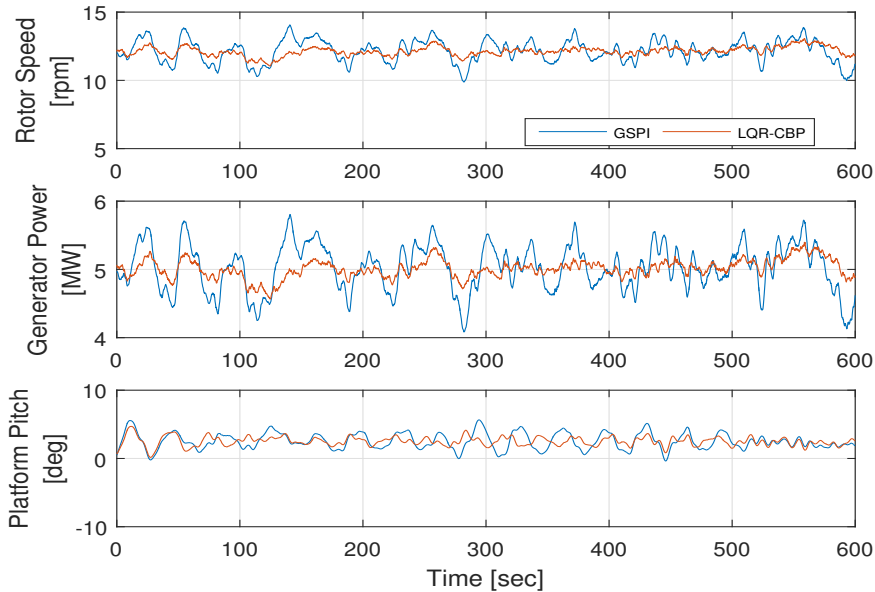

Figure 6.1: Comparison between the outputs obtained with GSPI and LQR–CBP

The results, shown in figure (6.1), have been achieved using the control variable time series presented in figure (6.2). In LQR–CBP control, the blade pitch is characterized by more oscillations with respect to the GSPI, thus using more the blade pitch actuators. The generator torque has more or less the same trend. No oscillations in the GSPI generator torque are due to the constant generator torque approach in region 3.
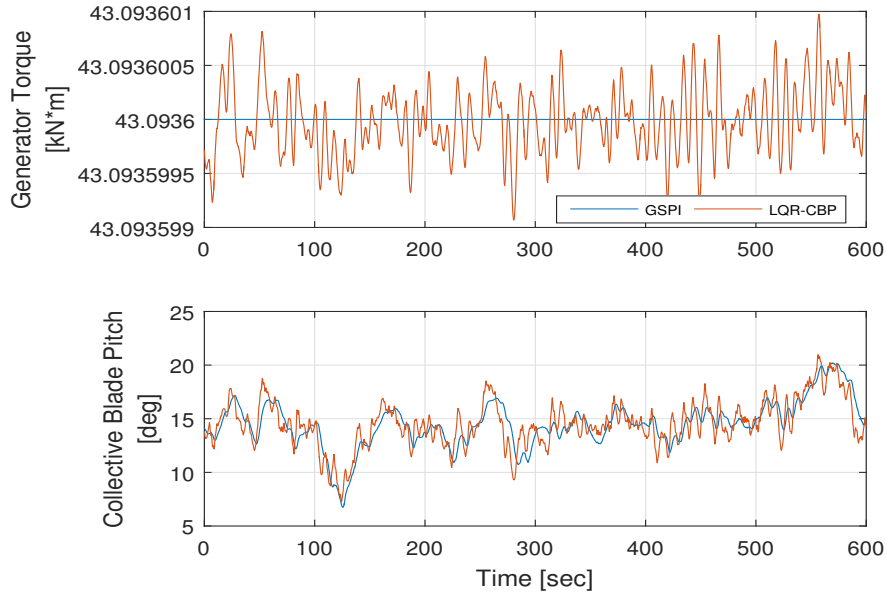
Figure 6.2: Comparison between the inputs obtained with GSPI and LQR–CBP

The tower-base fore-aft and side-to-side frequency content are presented in figure (6.3). The hight frequency contributions are the tower FA and SS first bending mode natural frequencies (~ 0.5 Hz). The low frequency variations are caused by the platform pitch and the platform roll motions, respectively. The figure shows an amplitude reduction at certain frequencies, especially at the platform pitch resonant frequency (0.034 Hz) for tower-base FA and at the platform roll natural frequency (0.034 Hz) for tower-base SS. These results are expected because in the LQR control the second objective was the tower FA and SS bending reduction.
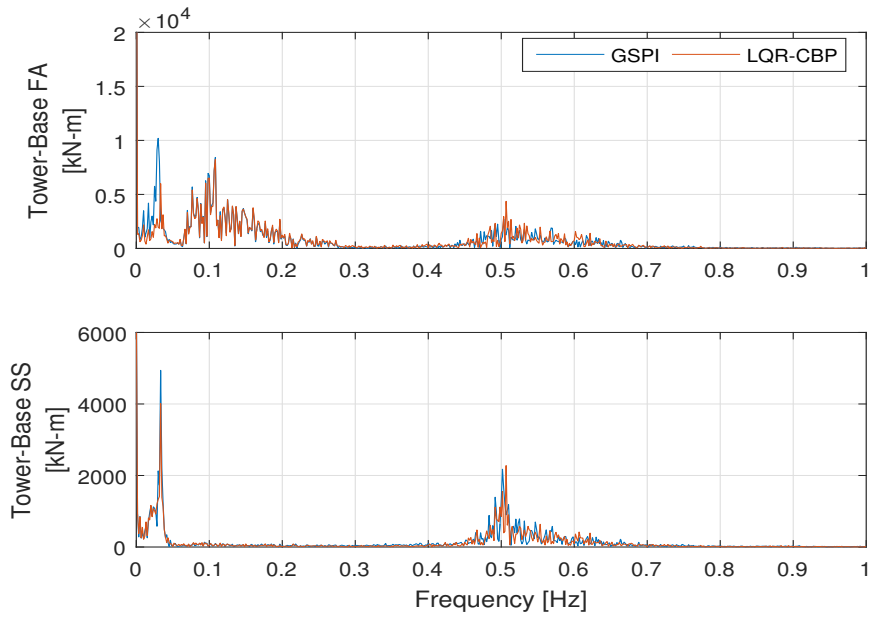
Figure 6.3: Tower-Base Bending moment frequency content comparision obteined with GSPI and LQR–CBP

The second comparison has been carried out between LQR–CBP and DAC–CBP. According to the same logic adopted in the previous part, the same parameters have been used for the analysis. As shown in figure (6.4) the three main outputs used to evaluate the different control qualities have been compared in terms of time series. DAC–CBP rotor speed and generator power present a bigger oscillation even though RMS values are lower than LQR–CBP, while the platform pitch remains basically unvaried.
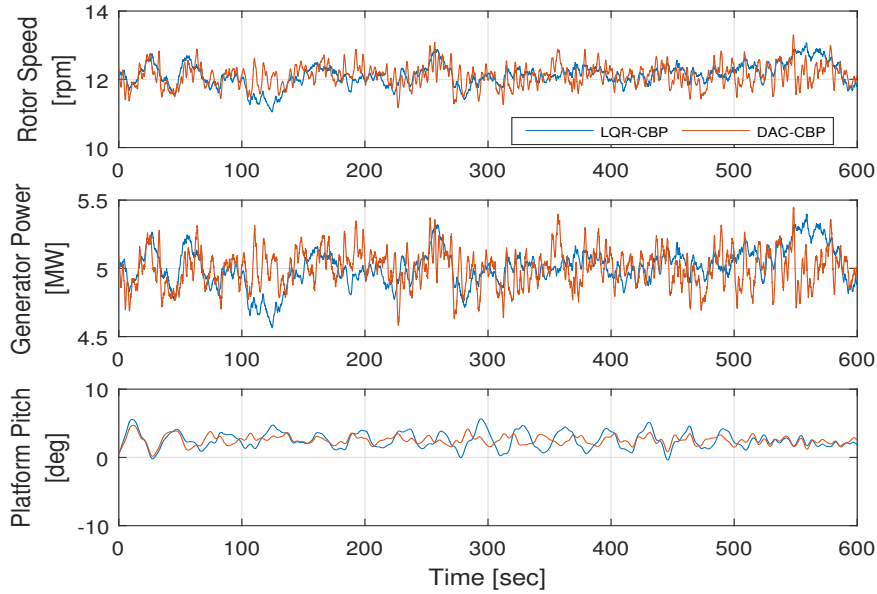

Figure 6.4: Comparison between the outputs obtained with LQR–CBP and DAC–CBP

The results, shown in figure (6.4), have been achieved using the control variable time series presented in figure (6.5). Using the DAC controller the collective blade pitch and the generator torque present more oscillations. This implies that the DAC uses the actuators with more frequency than the LQR–CBP. The bigger oscillations shown in figure (6.4) are probably caused by a higher utilization of the blade pitch actuators.
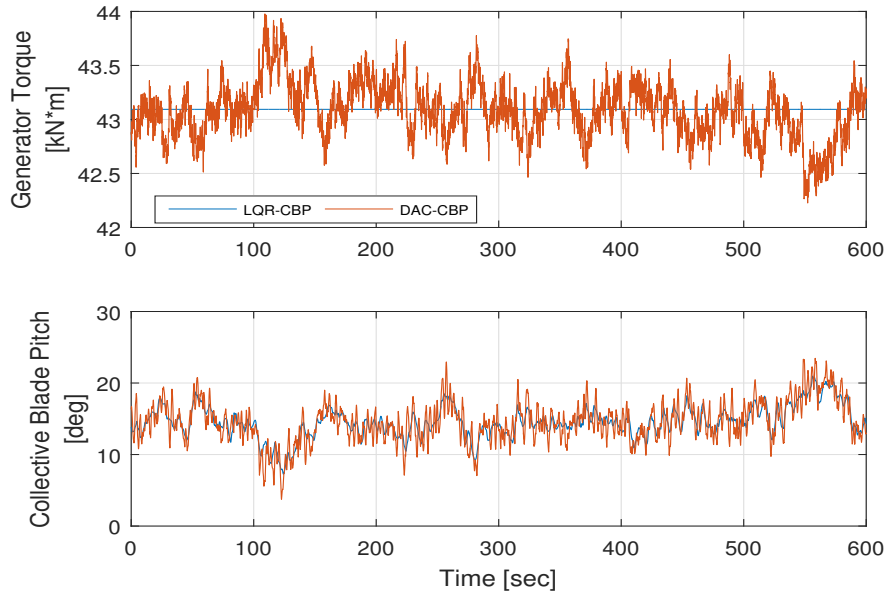

Figure 6.5: Comparison between the controllable inputs obtained with LQR–CBP and DAC–CBP

In this comparison, the tower-base fore-aft and side-to-side frequency content are presented in figure (6.6). DAC control has the capability to further reduce the frequency content both FA and SS. It is caused by its ability to decrease the platform motions.
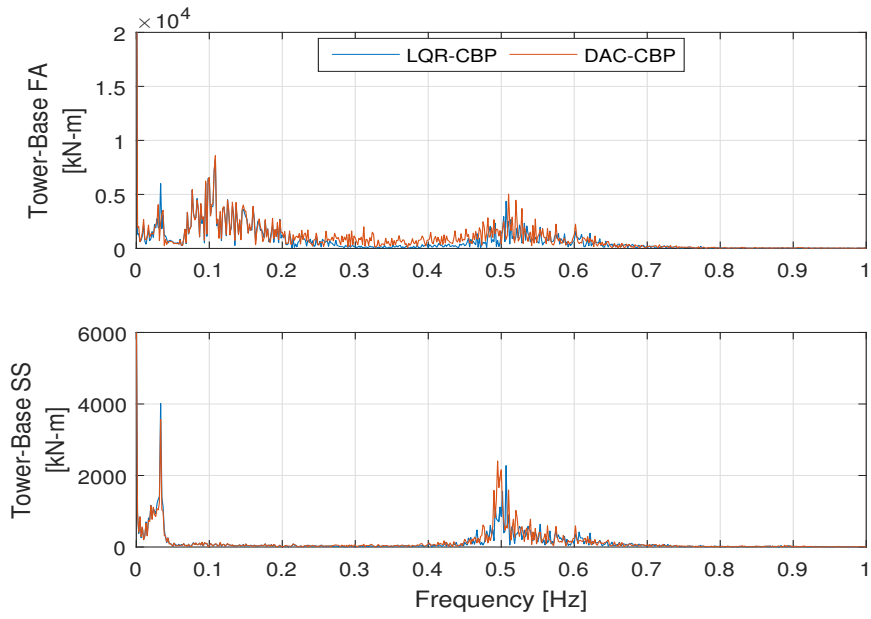
Figure 6.6: Tower-Base Bending moment frequency content comparision obteined with LQR–CBP and DAC–CBP

The third comparison has been done between LQR–CBP and LQR–IBP controllers. This analysis is based on the same parameters used in the previous comparisons. In particular, the three main outputs adopted to evaluate the different control qualities have been related in terms of time series, as shown in figure (6.7). Using the IBP controller, even thought the rotor speed and the generator torque present, more or less, the same trends, the platform pitch has a slightly smaller oscillation and a smaller peak value than the CBP controller. Creating asymmetric loads, best performances are achieved in reference outputs.
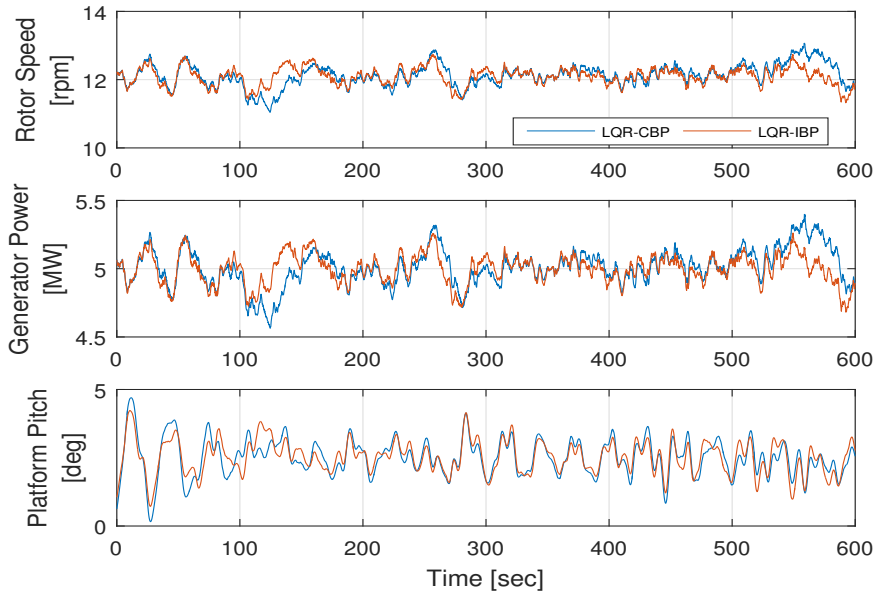
Figure 6.7: Comparison between the outputs obtained with LQR–CBP and LQR–IBP

The results, shown in figure (6.7), have been achieved using the control variable time series displayed in figure (6.8). Using the IBP controller the blade pitches present more oscillation than CBP controller. The differences reported in the figure are not very clear. Moreover, from the analysis reported in table (6.13), it is possible to note that the IBP blade pitch is characterized by a bigger RMS value. This means that the blade pitch actuators are used more intensively. However, the generator torque actuation remains somewhat limited in both controls.
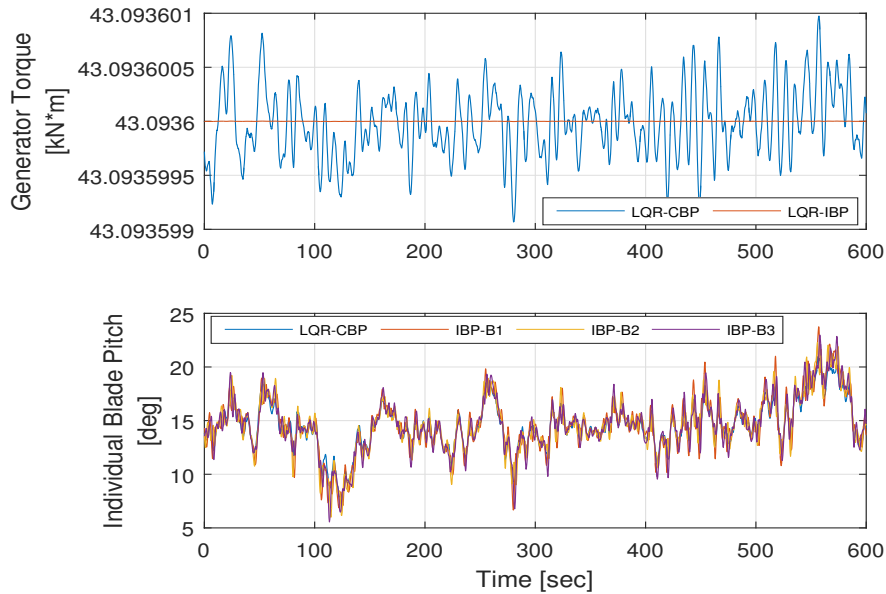

Figure 6.8: Comparison between the controllable inputs obtained with LQR–CBP and LQR–IBP

64

In the third comparison, the tower-base fore-aft and side-to-side frequency contents are presented in figure (6.9). The IBP controller decreases the tower-base FA contribution to the platform pitch natural frequency. Moreover, analysing the tower-base SS frequency content, it is possible to note that the IBP does not reduce the frequency contribution at the platform roll natural frequency, but equal frequency contribution is obtained with the GSPI controller. Although a reduction on tower SS oscillation was a secondary objective, this increase is probably due to the asymmetric load management introduced by the IBP controller.
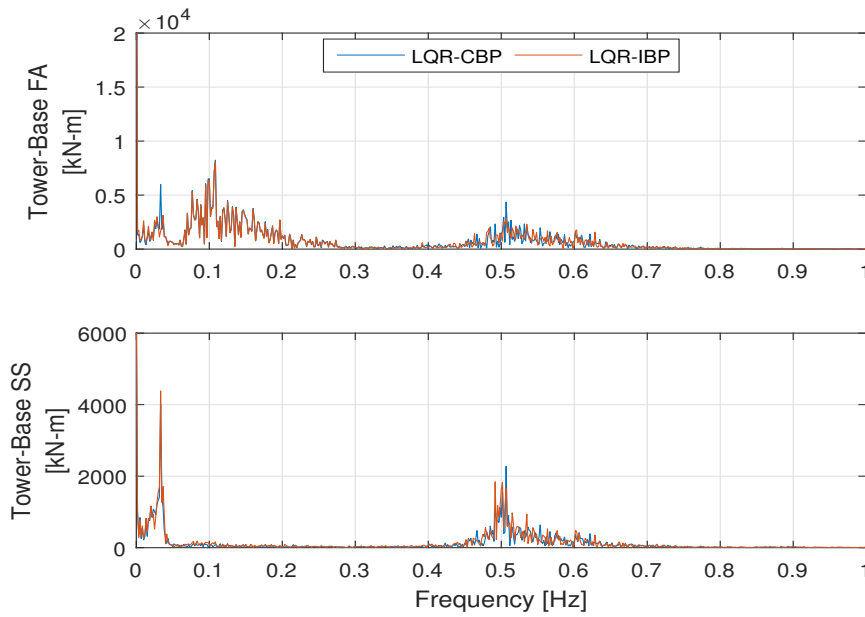
Figure 6.9: Tower-Base Bending moment frequency content comparision obteined with LQR–CBP and LQR–IBP

The fourth comparison has been carried out between LQR–IBP and DAC–IBP. In this analysis the same parameters used previously are shown. In figure (6.10) the three main outputs used to evaluate the different control qualities are compared in terms of time series. Similarly to the DAC–CBP, the feed-forward wind speed rejection provokes bigger oscillations than the LQR–IBP. Moreover it emerges that the platform pitch presents a slightly better trend. Details of the numeric comparison are depicted in table (6.13).
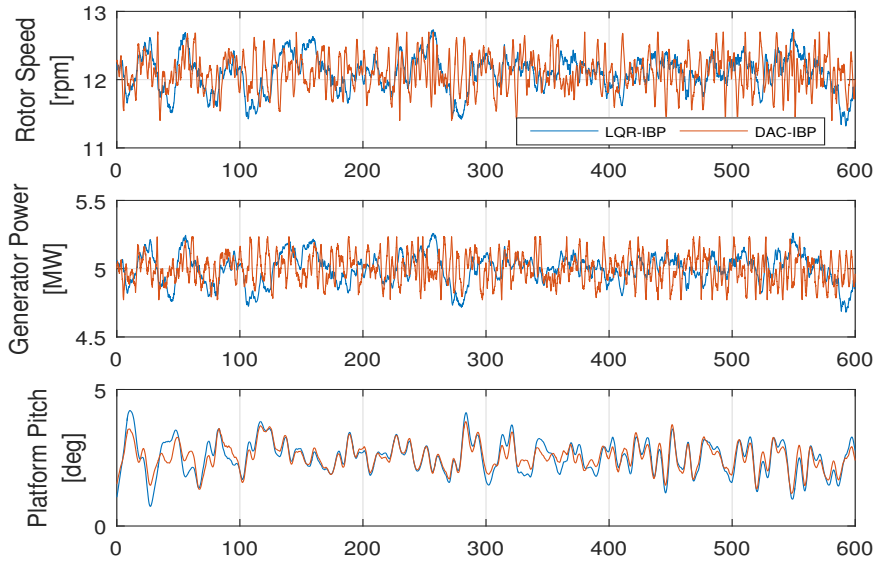
Figure 6.10: Comparison between the outputs obtained with LQR–IBP and DAC–IBP

The results, shown in figure (6.10), have been achieved using the control variable time series presented in figure (6.11). Only the blades pitches angles comparison are shown, because the generator torque controller does not present any particular variations. The DAC controller causes more oscillations than the IBP. These oscillations affect the rotor speed and thus also the generator power as figure (6.10) depicts.
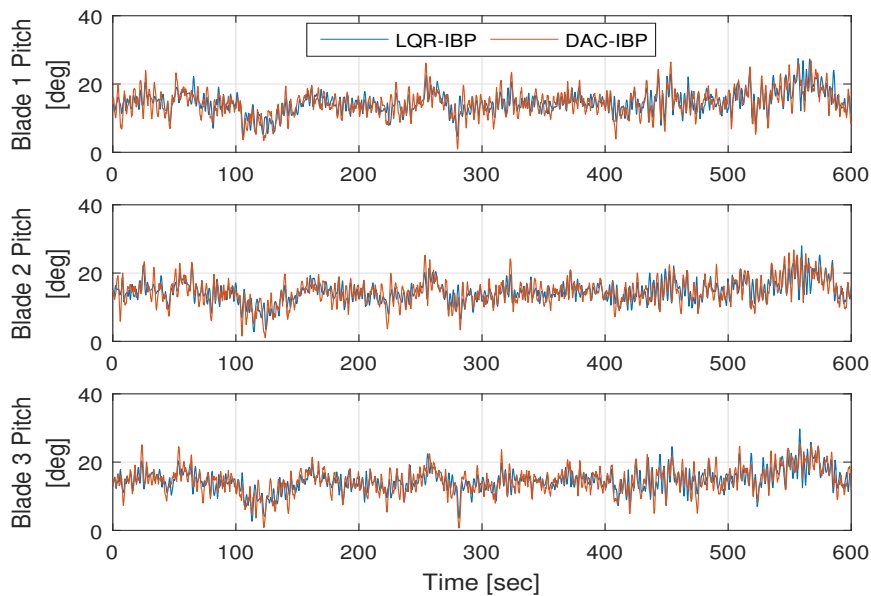
Figure 6.11: Comparison between the controllable blade pitch inputs obtained with LQR–IBP and DAC–IBP

In the tower-base fore-aft and side-to-side frequency contents are presented

in figure (6.12). These results are basically equal. However, it emerges that a further reduction in the platform pitch oscillation reduces the platform pitch natural frequency content in tower-base FA, whereas the height contribution in tower-base SS at the platform roll natural frequency is caused by the DAC incapability to reduce the platform roll oscillation. Such increase is probably caused by a hight blade pitch usage coupled with the asymmetric aerodynamic loads introduced by the IBP controller.

Figure 6.12: Tower-Base Bending moment frequency content comparision obteined with LQR–IBP and DAC–IBP

6.2   Normalized Indices Comparison

Figure 6.13: Normalized Performance index of the implemented controllers over the GSPI

All the achieved results can be compared by adopting the GSPI as reference. It can be noticed that the LQR–CBP controller presents better performance, reducing 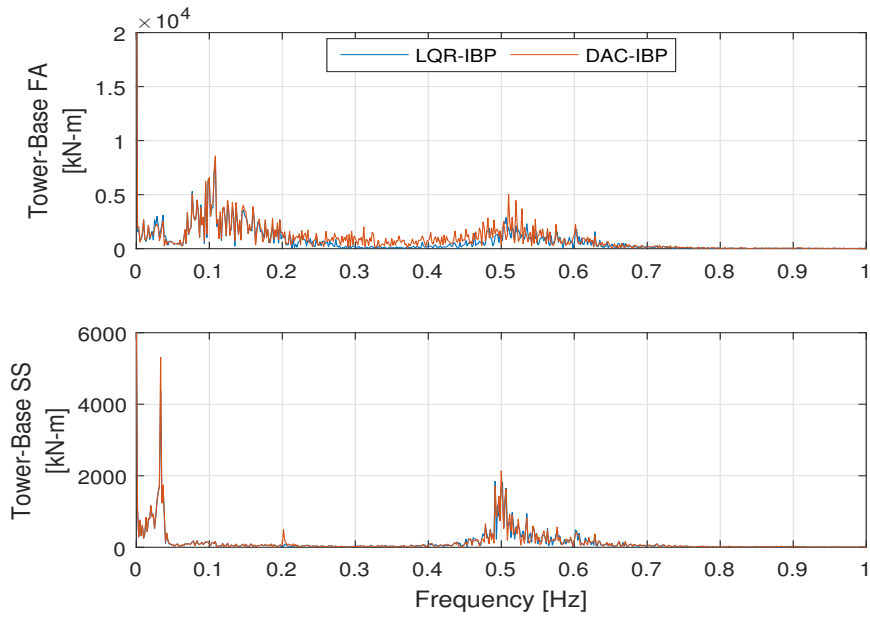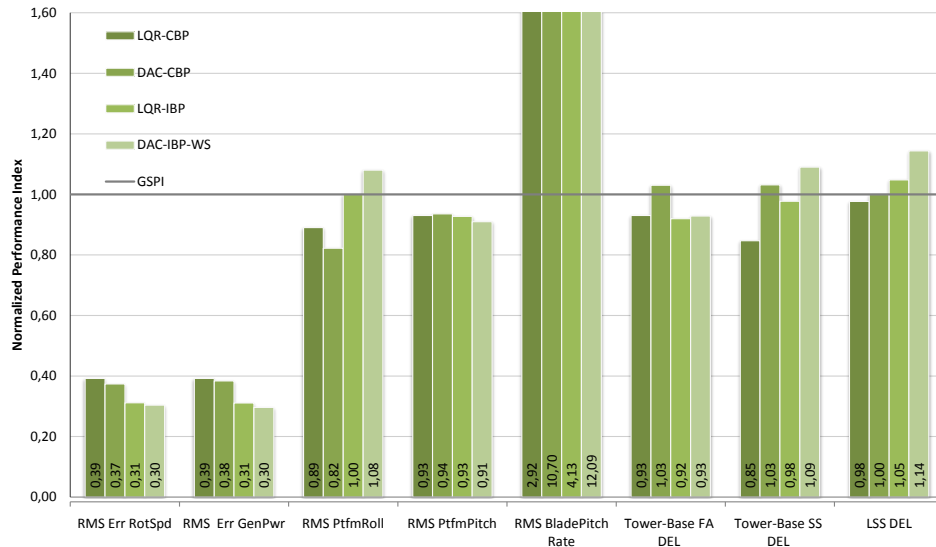the RMS of the rotor speed error by an average of 61%. This reduction implies a better quality of the power production. Improvements can also be seen in platform motions: the value of platform pitch RMS diminishes by an average of 7% and the platform roll RMS value reduces by an average of 11%. By introducing the tower bending modes in control objectives, DEL analysis produces an average reduction by 7% and 15% in tower fore-aft and side-to-side, respectively. Also the LSS DEL reports a decrease of 2%. The utilization of the LQR control produces a trend of the overall system, much better than the GSPI.

The DAC–CBP controller has the capability to reduce the RMS values of the rotor speed error and generator power error by an average of 63% and 62%, respectively. A reduction can also be seen in platform motions with a RMS values of the platform pitch and platform roll diminished by an average of 6% and 20%, respectively. About the tower-base DEL fatigue analysis, the fore-aft increases by 10% whereas the side-to-side increases by an average of 3%. In this case DEL analysis shows worst results, due to the high pitch actuators usage. Introducing the wind speed rejection in feed-forward achieve better performance in rotor speed, generator power, platform roll and platform pitch regulations but a worse result affects the loads analysis and actuator usage.

Further reductions are achieved by using the LQR–IBP controller, which has the capability to decrease by an average of 69% the RMS value of the rotor speed error, thus obtaining a better power quality. The platform rotation about its pitch axis is reduced by an average of 7%. The DEL analysis reports a reduction in FA and SS bending loads of the 8% and 2%, respectively. Again,

introducing the asymmetric loads increments the DEL LSS fatigue analysis by an average of 5%.

The DAC controller with wind share rejection achieved results comparable with LQR–IBP. DAC has the capability to reduce the RMS rotor speed error of 70%, thus improving the power quality. The platform pitch motion diminishes by an average of 9%. However, no reduction in platform roll oscillation affects tower-base SS DEL analysis, which reports an increase of 9%. Finally, the DEL analysis of the LSS bending reports an average increment of 14%.

Chapter 7

Conclusions and Further Developments

The spar-buoy platform achieves hydrostatic stability using a deep drafted ballast with three catenary mooring lines to remain in a fixed position. The deep draft of the spar-buoy increases the platform roll and pitch inertias, thus reducing their respective natural frequencies. A low platform pitch natural frequency affects the DOFs choice in the control design. Adding the platform surge DOF and the first tower fore-aft DOF to the linearized model, it captures all the essential features of the platform pitch dynamic.

A Gain Scheduled PI (GSPI) controller has been used as a reference to compare the performances of a State Feedback Controller (SFC) obtained with the Linear Quadratic Regulator (LQR). Initially it has been implemented using a collective blade pitch (CBP) and afterwards using an individual blade pitch (IBP). Furthermore, to minimize the wind speed perturbation effect, a Disturbance Accommodation Control (DAC) has been implemented with both the previous configurations. Using the DAC-CBP, only the hub-height uniform wind disturbance has been considered. On the contrary, the use of the DAC-IBP allows to take into account the wind share effect. The latter is a periodic effect that describes the horizontal increase of the wind speed according to the height.

The achieved results prove that using a multi-objective control improves the overall system trend, decreases the RMS value to the rotor speed error, and thus, increases the power quality. Furthermore, the state-feedback control (SFC) obtained with collective and individual blade pitch presents the capability to reduce the tower-base FA and SS fatigue loads, extending the wind turbine tower lifetime. Such results are very important because the main purpose is to produce a better power quality for the longest possible period. Using asymmetric aerodynamics loads helps prevent the controller from conflicting issues arising when rotor speed and platform pitch are regulated simultaneously. The IBP controller applied to a spar-buoy platform has a limited effectiveness due to a very low platform natural frequency, especially the platform pitch. Moreover, blade pitch saturations impose an upper limit to the controller gains, thus further limiting the IBP effectiveness.

The Disturbance Accommodating Control (DAC), obtained with CBP, allows a further reduction of the rotor speed error RMS value and of the platform motions RMS value. However, a hight actuators'usage affects the DEL fatigue on the tower-base FA and SS. Introducing the wind share effect on the DAC with IBP does not improve the performances, due to a hight blade pitch actuation that, coupled with the asymmetric loads, produces an extreme growth in the platform roll motions, thus increasing the tower-base DEL fatigue. Furthermore, the asymmetric aerodynamic load introduces a further fatigue load on the Low-Speed-Shaft bending moment.

As further developments of this dissertation, it would be interesting to expand the research field focusing on:

- Introducing the Light Detection and Ranging (LIDAR) system [9], which has the capability to measure the incoming wind speed before its interaction with the wind turbine rotor.

- Introduce a sea-wave estimator, aiming at rejecting the sea-wave disturbance.

- Introduce a Model Predictive Control (MPC) to take into account the control input constraints.

- Introduce a Hydro–Wind Kinetics Integrated Module for Renewable Energy Co-generation project, aiming at exploiting resources in an integrated manner thought the utilization of wind and marine current turbines in offshore plants.

Appendix A

Model Linearization

The geometry, coordinate system and DOFs of a three-bladed wind turbine offshore modelled with FAST and discussed in the chapters 2, 3 and 4 are used to develop the kinematic expressions for the entire structure [24]. These kinematic expressions are adopted to form kinetic expressions through Kane's equations. Kane's equations of motion, for a system with P generalized coordinates (DOF), use two sets of scalar quantities called generalized inertia forces, F_r^*, and generalized active forces, F_r, which are defined:

$$F_r = \sum_{i=1}^{w} {}^{E}v_r^{X_i} F^{X_i} + {}^{E}\omega_r^{N_i} M^{N_i} \qquad (r = 1, 2, \ldots, P) \qquad \text{(A.1)}$$

and

$$F_r^* = \sum_{i=1}^{w} {}^{E}v_r^{X_i}\left(-m_i {}^{E}a^{X_i}\right) + {}^{E}\omega_r^{N_i}\left(-{}^{E}\dot{H}^{N_i}\right) \qquad (r = 1, 2, \ldots, P) \qquad \text{(A.2)}$$

where it is assumed that for each rigid body, N_i, the active forces, F^{X_i} and M^{N_i}, are applied at the centre of point mass, X_i. The acceleration of the centre of mass point is given by ${}^{E}a^{X_i}$ and the time derivative of the angular moment of the rigid body in the inertial frame, E, is given by ${}^{E}\dot{H}^{N_i}$. The quantities ${}^{E}v_r^{X_i}$ and ${}^{E}\omega_r^{N_i}$ represent the partial lineal and angular velocities, respectively.

By a direct result of Newton's laws of motion, the Kane's equations of motion can be expressed as:

$$F_r + F_r^* = 0 \qquad (r = 1, 2, \ldots, P) \qquad \text{(A.3)}$$

These complete nonlinear equation of motion can we written as follows:

$$M(\underline{q}, \underline{u}, t)\underline{\ddot{q}} + \underline{f}(\underline{q}, \underline{\dot{q}}, \underline{u}, \underline{u_d}, t) = 0 \qquad \text{(A.4)}$$

where, M is the mass matrix, f is the nonlinear "forcing function" vector, $\underline{q}$ is the DOF displacements vector, $\underline{\dot{q}}$ is the DOF velocities vector, $\underline{\ddot{q}}$ is the acceleration vector, $\underline{u}$ is the control input vector, $\underline{u_d}$ is the wind input disturbance vector and t is the time. FAST numerically linearizes the equations (A.4) by perturbing each of the system variables about their respective operating point

values:

$$q = q_{op} + \Delta q$$
$$\dot{q} = \dot{q}_{op} + \Delta \dot{q}$$
$$\ddot{q} = \ddot{q}_{op} + \Delta \ddot{q} \tag{A.5}$$
$$u = u_{op} + \Delta u$$
$$u_d = u_{d_{op}} + \Delta u_d$$

Substituting these expressions into the motion equations and expanding as a Taylor series a linearized representation of equations results:

$$M\Delta\ddot{q} + C\Delta\dot{q} + K\Delta q = F\Delta u + F_d\Delta u_d \tag{A.6}$$

where

$$M = M_{op}\Big|_{op} \text{ is the mass matrix,}$$

$$C = \frac{\partial f}{\partial \dot{q}}\Big|_{op} \text{ is the damping matrix,}$$

$$K = \left[\frac{\partial M}{\partial q}\ddot{q} + \frac{\partial f}{\partial q}\right]\Big|_{op} \text{ is the stiffness matrix,} \tag{A.7}$$

$$F = -\left[\frac{\partial M}{\partial u}\ddot{q} + \frac{\partial f}{\partial q}\right]\Big|_{op} \text{ is the control input matrix, and}$$

$$F_d = -\frac{\partial f}{\partial u_d} \text{ is the wind input disturbance matrix.}$$

and about the system outputs representation is:

$$y = VelC\Delta\dot{q} + DspC\Delta q + D\Delta u + D_d\Delta u_d \tag{A.8}$$

where, $VelC$ is the output matrix velocity, $DspC$ is the output matrix displacement, D is the control input matrix and D_d is the wind input disturbance matrix.

Replacing the variables with this new configuration:

$$\Delta x = \begin{vmatrix} \Delta q \\ \Delta \dot{q} \end{vmatrix} \quad \text{and} \quad \Delta \dot{x} = \begin{vmatrix} \Delta \dot{q} \\ \Delta \ddot{q} \end{vmatrix} \tag{A.9}$$

It is possible to achieve the first order representation of the system

$$\Delta\dot{x} = A\Delta x + B\Delta u + B_d\Delta u_d$$
$$\Delta y = C\Delta x + D\Delta u + D_d\Delta u_d \tag{A.10}$$

where A is the state matrix, B is the control input matrix, B_d is the wind input disturbance matrix, C is the output matrix respect states contribution, D is the output matrix respect inputs contribution and D_d is the output matrix

respect the inputs disturbance contribution. These matrices were obtained from the second order representation, hence:

$$A = \begin{bmatrix} 0 & I \\ -M^{-1}K & -M^{-1}C \end{bmatrix}, \quad B = \begin{bmatrix} 0 \\ M^{-1}F \end{bmatrix},$$

$$B_d = \begin{bmatrix} 0 \\ M^{-1}F_d \end{bmatrix}, \quad \text{and} \quad C = \begin{bmatrix} DspC & VelC \end{bmatrix}$$

(A.11)

where I is the identity matrix, 0 is a zeros matrix whereas D and D_d matrices are the same between the first and second order representation.

Developing this thesis, it was considered as:

- Control Inputs:

  - Generator Torque
  - Collective Blade Pitch Angle
  - Individual Blade Pitch Angle

- Disturbance Inputs:

  - Horizontal hub-height wind speed
  - Vertical shear power-law exponent

- Measurable Outputs:

  - Rotor Speed
  - Generator Speed
  - Rotor Power
  - Tower-Top Fore-Aft displacement
  - Tower-Top Side-to-Side displacement
  - Platform Surge displacement
  - Platform Roll displacement
  - Platform Pitch displacement
  - Platform Yaw displacement
  - Blade Pitch Angles

Throughout FAST linearization it has been obtained a linear periodic model, namely getting a linear model where the matrices are a rotor azimuth function. A linear-time invariant model (LTI), as in [16], has been achieved considering the average of this matrices over the rotor azimuth angle. This simplification does not consider all the system periodicity but attempting both these control typologies were no noticeable differences between the performance of controllers (not reported here). Hence, to simplify the control model implementation it was used:

$$\dot{\underline{x}}(t) = A_{\text{avg}}\underline{x}(t) + B_{\text{avg}}\underline{u}(t) + B_{d_{\text{avg}}}\underline{u}_d(t)$$
$$\underline{y}(t) = C_{\text{avg}}\underline{x}(t) + D_{\text{avg}}\underline{u}(t) + D_{d_{\text{avg}}}\underline{u}_d(t)$$

(A.12)

where A_{avg}, B_{avg}, C_{avg}, D_{avg}, $B_{d_{\text{avg}}}$ and $D_{d_{\text{avg}}}$ are the average matrices.

Appendix B

Fatigue Analysis

The processing of the fatigue analysis data has been conducted using MLife [11]. MLife is a post–processor CAE, which uses a rainflow-counting algorithm to count Damage Equivalent Loads (DELs) for each simulation. It also applies a probability distribution and material properties to estimate lifetime damage and time to failure.

MLife extrapolates the damage cycles counts differently on the design load case (DLC) classification of the time-series data. In this dissertation it was considered only the design load cases for power production in normal operation (DLC 1.1). The parameters are summarized in table (B.1).

Wind		Wave			E	T	F
Model	Speed	Model	Height	Direction			
NTM	$V_{\text{in}} < V_{\text{hub}} < V_{\text{out}}$	NSS	$H_s = E[H_s|V_{\text{hub}}]$	$\xi = 0$	N.O.	U	1.25x1.2

Table B.1: Design Load Case for Power Production

where E is the Event, N.O. is the normal operation, T is the Load Type, U is the ultimate load, F is the load factor, NTM is the Normal Turbulence Model, NSS is Normal Sea State, V_{in} and V_{out} are the cut–in and cut–out wind speed, respectively.

B.1 Lifetime Damage

The program accumulates fatigue damage due to fluctuating loads over the wind turbine design life. These fluctuating loads are split into individual hysteresis cycles by matching minimum and maximum in each time series. Assuming that the damage accumulated linearly with each cycles and in according with Miner's Rule, it is possible to define the lifetime damage as:

$$D^{\text{Life}} = \sum_i \frac{n_i^{\text{Life}}}{N_i(L_i^{RF})} \qquad (B.1)$$

75

where n_i^{Life} is the extrapolated cycle counts, $N_i(\ )$ denotes the number of cycles to failure and L_i^{RF} is the load cycle range about a fixed mean value. The extrapolated cycle counts over the lifetime design was found as:

$$n_i^{\text{Life}} = f_i^{\text{Life}} n_i \tag{B.2}$$

where f_i^{Life} is the extrapolation factor depending on: wind turbine availability, DLC selected, mean wind speed and Weibull distribution, see [13] for a more detailed formulation.

The relationship between cycles to failure (S–N curve) and load range is modelled by:

$$N_i = \left(\frac{L^{ult} - |L^{MF}|}{\left(\frac{1}{2} L_i^{RF}\right)} \right)^m \tag{B.3}$$

where L^{MF} is the fixed load-mean, L^{ult} is the ultimate design load and m is the Whöler exponent. The ultimate loads were calculated with MExtremes [12]. The Whöler exponent is specific to the component under consideration, in this project it was used: $m = 4$ for tower and platform and $m = 10$ for blades.

B.1.1 Goodman Exponent

The equation above assumes that the fatigue cycles occur over a fixed load mean. However, the actual load cycles occur over a spectrum of load means. To account this correction it must be used the Goodman correction expressed by the following expression:

$$L_i^{RF} = L_i^R \left(\frac{L^{ult} - |L^{MF}|}{L^{ult} - |L_i^M|} \right) \tag{B.4}$$

where L_i^R is the ith cycle's range about a load mean of L_i^M. In this equation the Goodman exponent is equal to one.

B.2 Time Until Failure

In addition to the lifetime damage calculation, it is possible to determine the time until failure. Since a failure occurs when $D^{\text{Life}} = 1$, the time until failure, T^{Fail}, is simply the ratio of the design lifetime over the accumulated damage.

$$T^{\text{Fail}} = \frac{T^{\text{Life}}}{D^{\text{Life}}} \tag{B.5}$$

where T^{Life} is the wind turbine lifetime design in seconds corresponding to 20 years.

B.3 Damage Equivalent Loads

Damage Equivalent Loads (DELs) is a constant amplitude fatigue load occurring at a fixed load-mean and frequency. It produces the equivalent damage

as the variable spectrum such that:

$$D_j = \sum_i \frac{n_{ij}}{N_{ij}} = \frac{n_j^{eq}}{N_i^{eq}} \tag{B.6}$$

$$n_j^{eq} = f^{eq}\, T_j \tag{B.7}$$

$$N_j^{eq} = \left(\frac{L^{\mathrm{ult}} - |L^{\mathrm{MF}}|}{\left(\frac{1}{2}\mathrm{DEL}_j^{\mathrm{F}}\right)}\right)^m \tag{B.8}$$

where T_j is the elapsed time of the jth time series, f^{eq} is the DEL frequency set to 1 Hz, n_j^{eq} is the total equivalent fatigue counts for j^{th} time series, N_j^{eq} is the equivalent number of cycles until failure for j^{th} time series and DEL_j^{F} is the DEL for the jth time series. Solving the equation (B.8) for DEL_j^{F}, results:

$$DEL_j^{\mathrm{F}} = \left(\frac{\sum_i \left(N_{ij}(L_{ij}^{\mathrm{RF}})^m\right)}{n_j^{eq}}\right)^{\frac{1}{m}} \tag{B.9}$$

This term will be used in the controller comparative analysis to evaluate the fatigue load on the wind turbine.

Bibliography

[1] IEC 61400-3, ed. *Wind Turbines - Part 3: Design Requirements for Offshore Wind Turbines*. Technical Report. International Electrotechnical Commission (IEC), 2006.

[2] G. Corbetta A. Ho A. Mbistrova. *The European offshore wind industry – key trends and statistics 2015*. Technical Report. The European Wind Energy Association, 2015.

[3] Marzorati A. *Modellistica e Controllo di turbine offshore per acque profonde*. Tesi di laurea Magistrale. Politecnico di Milano, 2012.

[4] G. Bir. *Multiblade Coordinate Transformation and Its Application to Wind Turbine Analysis*. Conference Paper. NREL, 2008.

[5] G. Bir. *User's Guide to MBC3 (Multi-Blade Coordinate Transformation Utility for 3-Bladed Turbines)*. Technical Report. NREL, 2008.

[6] L. Kilcher B.J. Jonkman. *TurbSim User's Guide*. Technical Report. NREL, 2012.

[7] Newman J.N. C.H. Lee. *WAMIT User Manual*. Technical Report. MIT, 2006.

[8] A. Craig Hansen David J. Laino. *AeroDyn User's Guide*. Technical Report. NREL, 2002.

[9] L.Y. Pao E. Simley. *LIDAR Wind Speed Measurement of Evolving Wind Fields*. Technical Report. NREL, 2012.

[10] A.S. Wright L.J. Fingersh. *Advanced Control Design for Wind Turbines - Part I: Control Design, Implementation and Initial Test*. Technical Report. NREL, 2008.

[11] M. Buhl Jr. G.J. Hayman. *Mlife User's Guidel for Version 1.00*. Technical Report. NREL, 2012.

[12] G.J. Hayman. *MExtremes Theory Manual for Version 1.00*. Technical Report. NREL, 2015.

[13] G.J. Hayman. *Mlife Theory Manual for Version 1.00*. Technical Report. NREL, 2012.

[14] Karl Stol Hazim Namik. "Disturbance Accommodating Control of Floating Offshore Wind Turbines". In: *American Institute of Aeronautics and Astronautics* (2009).

[15] Karl Stol Hazim Namik. "Individual Blade Pitch Control of a Spar-Buoy Floating Wind Turbine". In: *IEEE transactions on control systems technology, vol. 22* (2014).

[16] Karl Stol Hazim Namik. "Individual Blade Pitch Control of Floating Offshore Wind Turbines on a Tension Leg Platform". In: *American Institute of Aeronautics and Astronautics* (2010).

[17] J.H. Horlock. *Actuator disc theory: discontinuities in thermo fluid dynamics.* International series of engineering fluid dynamics. McGraw-Hill, 1978. ISBN: 9780070303607. URL: https://books.google.it/books?id=0a5RAAAAMAAJ.

[18] S. Butterfield J. Jonkman. *Definition of a 5-MW Reference Wind Turbine for Offshore System Development.* Technical Report. NREL, 2009.

[19] Marshall L. Buhl Jr. Jason M. Jonkman. *FAST User's Guide.* Technical Report. NREL, 2005.

[20] A.N. Robertson J.M. Jonkman and G.J. Hayman. *HydroDyn User's Guide and Theory Manual.* Technical Report. NREL, 2013.

[21] M.L. Buhl J.M. Jonkman. *New Developments for the NWTC's FAST Aeroelastic HAWT Simulator.* Conference Paper. NREL, 2004.

[22] J. Jonkman. *Definition of the Floating System for Phase IV of OC3.* Technical Report. NREL, 2010.

[23] J.M. Jonkman. *Dynamics Modeling and Loads Analysis of an Offshore Floating Wind Turbine.* Technical Report. NREL, 2007.

[24] J.M. Jonkman. *Modeling of the UAE Wind Turbine for Refinement of the FAST_AD.* Technical Report. NREL, 2003.

[25] R. Scattolini L. Magni. *Complementi di Controlli Automatici.* Ed. by Pitagora Editrice. 2006.

[26] J.G. Leishman. *Principles of Helicopter Aerodynamics.* Cambridge Aerospace Series. Cambridge University Press, 2002. ISBN: 9780521523967. URL: https://books.google.cz/books?id=-PnV2JuLZi4C.

[27] Denis Matha. *Model Development and Loads Analysis of an Offshore Wind Turbine on a Tension Leg Platform, with Comparison to Other Floating Turbine Concept.* Technical Report. NREL, 2009.

[28] Patrik J. Moriarty. *AeroDyn Theory Manual.* Technical Report. NREL, 2004.

[29] Hazim Namik. "Individual Blade Pitch and Disturbance Accommodating Control of Floating Offshore Wind Turbines". PhD thesis. The University of Auckland, 2012.

[30] M. Hansen H. Hansen A. Larsen T.J. Oye S. Sorensen. *Control Design for a Pitch-Regulated, Variable-Speed Wind Turbine.* Technical Report. Risø National Laboratory Information Service Department, 2005.

[31] Statoil. *Hywind Scotland Pilot Park Project.* Technical Report. Statoil, 2015.

[32] Robert H. Stewart. *Chapter 16 - Ocean Waves.* 2006. URL: http://oceanworld.tamu.edu/resources/ocng%5C_textbook/chapter16/chapter16%5C_04.htm.

[33] T.D. Hanson T.J. Larsen. "A method to avoid negative damping low frequent tower vibrations for a floating, pitch controlled wind turbine". In: *IOP Science* (2007).

[34] A.S. Wright. *Modern Control Design for flexible Wind Turbines.* Technical Report. NREL, 2004.